J. Fluid Mech. (2001), *vol.* 432, *pp.* 31–68. Printed in the United Kingdom

Core–annular flow in a periodically constricted circular tube. Part 1. Steady-state, linear stability and energy analysis

By CHARALAMPOS KOURIS AND JOHN TSAMOPOULOS†

Laboratory of Computational Fluid Dynamics, Department of Chemical Engineering, University of Patras, Patras 26500, Greece
e-mail: tsamo@chemeng.upatras.gr

(Received 24 January 2000 and in revised form 29 August 2000)

The concentric, two-phase flow of two immiscible fluids in a tube of sinusoidally varying cross-section is studied. This geometry is often used as a model to study the onset of different flow regimes in packed beds. Neglecting gravitational effects, the model equations depend on five dimensionless parameters: the Reynolds and Weber numbers, and the ratios of density, viscosity and volume of the two fluids. Two more dimensionless numbers describe the shape of the solid wall: the constriction ratio and the ratio of its maximum radius to its period. In addition to the effect of the Weber number, which depends on both the fluid and the flow, the effect of the Ohnesorge number J has been examined as it characterizes the fluid alone. The governing equations are approximated using the pseudo-spectral methodology while the Arnoldi algorithm has been implemented for computing the most critical eigenvalues that correspond to axisymmetric disturbances. Stationary solutions are obtained for a wide parameter range, which may exhibit flow recirculation at the expanding portion of the tube. Extensive calculations are made for the dependence of the neutral stability boundaries on the various parameters. In most cases where the steady solution becomes unstable it does so through a Hopf bifurcation. Exceptions to this are cases where the viscosity ratio is $O(10^{-3})$ and, then, the most unstable eigenvalue remains real. Generally, steady core–annular flow in this geometry is more susceptible to instability than in a straight tube and, in similar ranges of the parameters, it may be generated by different mechanisms. Decreasing the thickness of the annular fluid, inverse Weber number or the Ohnesorge number or the density of the core fluid stabilizes the flow. For stability reasons, the viscosity ratio must remain strictly below unity and it has an optimum value that maximizes the range of allowed Reynolds numbers.

1. Introduction

Concurrent two-phase flow arises in many important scientific and technological disciplines. For example, concurrent two-phase flow of hydrogen and hydrocarbons takes place through millimetre-scale tortuous passages created by catalytic particles, which promote reforming of oil and its byproducts in certain trickle bed reactors. In this application inertial, viscous and capillary forces are all comparable in magnitude and none can be neglected *a priori* (de Santos, Melli & Scriven 1991; Melli *et al.* 1990).

† Author to whom correspondence should be addressed.

In the last fifteen years, considerable effort has been put into understanding the core–annular flow of two liquids, a technique used to facilitate the transport of viscous oil through a pipeline by lubricating it with a low-viscosity liquid such as water (Joseph & Renardy 1993). Finally, two fluids flow concurrently through corrugated and narrow passages in processes aimed at recovering oil from sedimentary rocks by injecting primarily water or steam (Payatakes 1982). Different flow regimes arise in all these applications in which either one or both phases may be continuous or discontinuous and the flow may be steady, oscillatory or chaotic depending on the operating conditions.

In the case of a trickle bed reactor, it is well known that the different flow regimes greatly affect the reactor parameters, namely pressure drop, heat and mass transfer coefficients, reaction rate and liquid holdup. Therefore, the prediction of the onset of these flow regimes is critical in reactor design and operation. Kouris *et al.* (1998) predicted that the effectiveness factors of the chemical reactions in hydrodesulphurization processes are greatly enhanced when the reactor operates in the pulsing flow regime, owing to the increased averaged mass transfer coefficient of the gas phase. Because of their importance, the various flow regimes in packed beds have been studied extensively both theoretically and experimentally. Macroscopic models of two-phase flow in packed beds, based on volume-averaged equations of motion have been developed and solved. A comprehensive review of the related literature up to 1991 is given in de Santos *et al.* (1991).

It is believed that the fundamental mechanisms that give rise to the different flow regimes are rooted at the scale of the pore, where the two phases flow and compete for the available space. Many experimental studies have been performed to visualize the microscale hydrodynamics, see for example Melli *et al.* (1990). These authors, in particular, have studied the two-phase concurrent down-flow of air and water in a host of geometries ranging from model arrangements to single vertical constricted tubes. A popular approximation of the tortuous paths in a packed bed is an array of parallel conduits of circular cross-section, the radius of which varies sinusoidally in the axial direction. Although this configuration cannot describe latitudinal dispersion in the bed or exchange of fluids between nearby conduits, it simulates the converging–diverging character of the flow in an actual packed bed, which is important and cannot be described by a straight tube. This model has been used extensively for simulating the single-phase flow of both Newtonian (Deiber & Schowalter 1979; Lahbabi & Chang 1986, and references therein) and non-Newtonian fluids (e.g. Pilitsis & Beris 1989). However, no study of two-phase flow in a periodically constricted tube (PCT) has been reported so far.

On the other hand, many theoretical studies of two-phase flow inside straight tubes or between parallel plates using standard methods of linear stability theory have been reported. First, Yih (1967) studied the stability with respect to long waves of plane Couette flow of two layers separated by a planar interface. He suppressed the effects of gravity and density differences and examined the viscosity difference between the two fluids. He found that this flow arrangement is unstable to long-wave disturbances irrespective of the value of the Reynolds number. Hickox (1971) studied the stability of Poiseuille flow of two liquids when the less-viscous fluid is centrally located, including the effects of surface tension and gravity, and showed that all such flows are unstable. Such arrangements of parallel flows of immiscible fluids in a cylindrical tube in which one fluid moves in the core of the tube and the other one in the annulus are called core–annular flows (CAF). Hooper & Boyd (1983) considered the stability of Couette flow of two fluids separated by a plane layer in an unbounded and infinite region. They found that the flow is always unstable to very short waves when surface tension

is neglected. Surface tension stabilizes the shortest waves. Furthermore, Yiantsios & Higgins (1988) studied the stability of plane Poiseuille flow of two superposed fluids, identifying not only the modes reported by Yih (1967), but also shear modes which arise at a high Reynolds number and are associated with Tollmien–Schlichting waves. Russo & Steen (1989), considering the stability of an annular liquid film flowing down a rod with a free surface, have shown that shear can stabilize capillary breakup, if the film is thin enough. This extends the earlier analysis by Xu & Davis (1985).

D. Joseph, Y. Renardy, M. Renardy and co-workers have achieved important advances in CAF over the last fifteen years. Early on, Joseph, Renardy & Renardy (1984) studied the stability of Poiseuille flow of two fluids with different viscosities and they found that this flow with an interface of constant radius is stable provided that the layer of fluid on the wall of the pipe is less viscous and thin enough. Renardy (1985) studied the stability of layered Couette flow to disturbances of arbitrary wavelength. Preziosi, Chen & Joseph (1989) studied the stability of CAF and found remarkable agreement between their results from linear stability theory and older experiments (Charles, Govier & Hodgson 1961; Oliemans & Ooms 1986). Linear stability, in spite its limitations, has been quite successful in the past in accurately predicting, for example, the capillary instability of jets (Rayleigh 1879), annular menisci (Tsamopoulos, Poslinski & Ryan 1988) and instabilities in other single-fluid flows (Chandrasekhar 1981). Hu & Joseph (1989), in addition to performing linear stability analysis of two- and three-layered concentric fluids, calculated the energy associated with the various mechanisms and, thus, identified the driving mechanism that leads to instability, which in turn depends on the parameter values. This idea was employed earlier by Hooper & Boyd (1983) and later used to classify instabilities in a variety of flows by Boomkamp & Miesen (1997). Hu & Patankar (1995) studied the stability of CAF of water and oil in a circular pipe with respect to non-axisymmetric disturbances and Huang & Joseph (1995) studied the stability of eccentric core-annular flow. Papageorgiou, Maldarelli & Rumschitzki (1990) studied the nonlinear stability of CAF in straight tubes assuming that the deviation of the fluid interface from its initial value is small compared to the thickness of the annular fluid and that, in turn, is small compared to the radius of the pipe. They found that in the limit of slow flow and moderate surface tension the contribution of the viscosity stratification is only dispersive, whereas in the case of fast flow and strong surface tension the contribution of the viscosity difference can be either stabilizing or destabilizing. Kerchman (1995) extended the analysis of Papageorgiou, Maldarelli & Rumschitzki (1990) by removing the constraint that the deviation of the interface from its initial value is quite small. Finally, Joseph *et al.* (1997) give additional references on CAF in a straight tube in their review of the subject.

In this work we use the periodically constricted tube to represent the geometry in a packed-bed reactor in which concentric two-phase flow takes place. Our goal is to predict the operating conditions under which travelling waves arise as bifurcations of perfect CAF and signal the onset of different flow regimes, and to examine how our results are related to previous theoretical results reported for the case of a straight tube. Neglecting gravity, the governing equations, given in § 2, depend on five dimensionless parameters: the Reynolds and Weber numbers, and the ratios of density, viscosity and volume of the two liquids. Two more dimensionless numbers characterize the geometry of the tube wall: the constriction ratio, i.e. the ratio of the minimum to the maximum radius of the tube, and the ratio of its maximum radius to its length. Following the necessary transformations, § 3, the method for obtaining the steady solutions and examining their stability is presented in § 4. In addition, we calculate the various contributions to the energy budget, § 5. Since instability is also

manifested by the increase of kinetic energy of an initially small disturbance with time, comparing contributions to this balance coming from the bulk of either fluid or from interfacial terms which are related either to capillarity or viscosity contrast indicates the dominant mechanism of instability. An additional mechanism for instability exists in the case of a constricted tube compared to those in a straight tube: the interface of the base state varies in the axial direction and so it has two radii of curvature modifying the capillary forces and generating additional friction against the flow. The governing equations are solved using the psuedo-spectral method, § 6. According to it, every dependent variable is approximated by Chebyshev polynomials in the radial direction and Fourier modes in the axial direction. For both stationary calculations and linear stability, convergence of results is checked numerically by comparison with analytical solutions or previous numerical studies, which are valid in limiting cases, § 7. New stationary solutions are obtained for a wide parameter range, § 8. The boundaries of the regions of linear stability of CAF in constricted tubes are identified by calculating the eigenvalues of the system using the Arnoldi algorithm. Temporal stability of the axisymmetric base state is examined to two-dimensional disturbances using the streamfunction–vorticity formulation, § 9. Conclusions are drawn in § 10.

2. Governing equations

We examine the incompressible core–annular flow (CAF) of two Newtonian fluids in a pipe of circular cross-section the radius of which, $\hat{R}_2$, varies sinusoidally between the values $\hat{R}_{min}$ and $\hat{R}_{max}$ with axial wavelength $\hat{L}$, see figure 1. The equation that governs the radial distance of the solid wall from the axis of symmetry is

$$\hat{R}_2(\hat{z}) = \frac{\hat{R}_{max} + \hat{R}_{min}}{2} - \frac{\hat{R}_{max} - \hat{R}_{min}}{2} \cos\left(2\pi \frac{\hat{z}}{\hat{L}}\right), \quad 0 \leqslant \hat{z} \leqslant N\hat{L}, \tag{2.1}$$

where, in general, the caret denotes dimensional quantities and N denotes the number of the repeated geometrical units that are considered to form a long enough section of the constricted tube. The pipe axis is located at $\hat{r} = 0$. The core region, $0 \leqslant \hat{r} \leqslant \hat{R}_1(\hat{z}, \hat{t})$, is occupied by the first liquid with viscosity and density $\hat{\mu}_1$ and $\hat{\rho}_1$, respectively, while the second liquid $(\hat{\mu}_2, \hat{\rho}_2)$ is located in the surrounding annulus, $\hat{R}_1(\hat{z}, \hat{t}) \leqslant \hat{r} \leqslant \hat{R}_2(\hat{z})$. The position vector of the common fluid/fluid interface is defined by

$$\hat{\boldsymbol{R}}_1 = \boldsymbol{e}_r \hat{R}_1(\hat{z}, \hat{t}) + \boldsymbol{e}_z \hat{z}. \tag{2.2}$$

The corresponding components of the velocity vector of each fluid are denoted as

$$\hat{\boldsymbol{U}}_i = (\hat{U}_i, \hat{V}_i, \hat{W}_i) = \boldsymbol{e}_r \hat{U}_i + \boldsymbol{e}_\theta 0 + \boldsymbol{e}_z \hat{W}_i, \tag{2.3}$$

where $(\hat{r}, \hat{\theta}, \hat{z})$ are the cylindrical coordinates, $(\boldsymbol{e}_r, \boldsymbol{e}_\theta, \boldsymbol{e}_z)$ are the corresponding unit vectors and $\hat{t}$ denotes the time variable. Neglecting gravity, the equations that govern the motion of both fluids as well as the fluid/fluid interface, are the following:

$$\nabla \cdot \hat{\boldsymbol{U}}_i = 0, \tag{2.4}$$

$$\hat{\rho}_i \frac{\mathrm{D}\hat{\boldsymbol{U}}_i}{\mathrm{D}\hat{t}} = -\nabla \hat{P}_i + \nabla \cdot \hat{\boldsymbol{\tau}}_i \tag{2.5}$$

$$\frac{\mathrm{D}\hat{\boldsymbol{R}}_1}{\mathrm{D}\hat{t}} = \hat{\boldsymbol{U}}_i(\hat{R}_1(\hat{z}, \hat{t}), \hat{z}, \hat{t}), \tag{2.6}$$

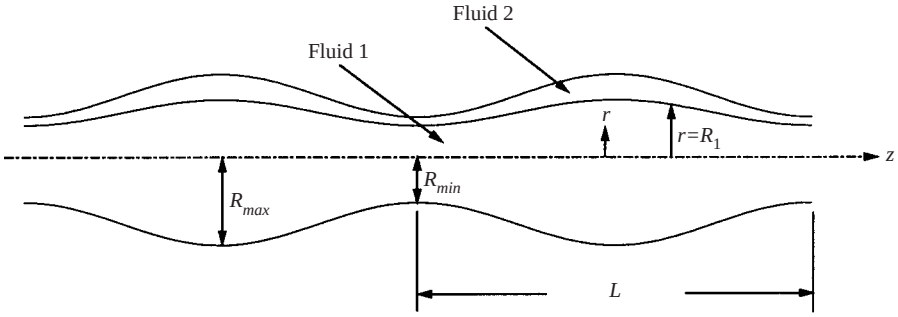

FIGURE 1. Schematic presentation of the flow geometry showing the tube wall and the fluid/fluid interface.

where $i = 1$ corresponds to the core and $i = 2$ to the annular fluid. The gradient operator in cylindrical coordinates and the material derivative are defined in the usual manner:

$$\nabla(\cdot) = \boldsymbol{e}_r \frac{\partial(\cdot)}{\partial \hat{r}} + \frac{\boldsymbol{e}_\theta}{\hat{r}} \frac{\partial(\cdot)}{\partial \hat{\theta}} + \boldsymbol{e}_z \frac{\partial(\cdot)}{\partial \hat{z}}, \tag{2.7}$$

$$\frac{\mathrm{D}(\cdot)}{\mathrm{D}\hat{t}} = \frac{\partial(\cdot)}{\partial \hat{t}} + \hat{\boldsymbol{U}}_i \cdot \nabla(\cdot). \tag{2.8}$$

Equations (2.4)–(2.6) have to be solved subject to the following boundary conditions:

(i) The velocity field is bounded at the axis of symmetry, zero at the tube wall and continuous at the fluid/fluid interface. At the same interface the viscous stresses exerted by either fluid are balanced by capillarity:

$$\hat{\boldsymbol{U}}_1 \quad \text{finite on} \quad \hat{r} = 0, \tag{2.9}$$

$$\hat{\boldsymbol{U}}_2 = \boldsymbol{0} \quad \text{on} \quad \hat{r} = \hat{R}_2(\hat{z}), \tag{2.10}$$

$$\|\hat{\boldsymbol{U}}\| = \boldsymbol{0} \quad \text{on} \quad \hat{r} = \hat{R}_1(\hat{z}, \hat{t}), \tag{2.11}$$

$$(-\|\hat{P}\| - 2\hat{H}\hat{T})\boldsymbol{n} + \|\hat{\boldsymbol{\tau}}\| \cdot \boldsymbol{n} = \boldsymbol{0} \quad \text{on} \quad \hat{r} = \hat{R}_1(\hat{z}, \hat{t}), \tag{2.12}$$

where $\hat{\boldsymbol{\tau}}_i = \hat{\mu}_i(\nabla \hat{\boldsymbol{U}}_i + \nabla \hat{\boldsymbol{U}}_i^T)$ is the extra stress tensor of each fluid, $2\hat{H} \equiv -\nabla \cdot \boldsymbol{n}|_{\hat{r}=\hat{R}_1}$ is twice the mean surface curvature of the fluid/fluid interface, $\hat{T}$ is the coefficient of the surface tension, $(\boldsymbol{n}, \boldsymbol{t})$ are the unit vectors normal and tangent to the surface $\hat{r} = \hat{R}_1(\hat{z}, \hat{t})$ respectively, while the normal vector is directed from fluid 1 to fluid 2 and $\|\cdot\| \equiv (\cdot)_1 - (\cdot)_2$ denotes the jump of the bracketed quantitiy over $\hat{r} = \hat{R}_1(\hat{z}, \hat{t})$.

(ii) In addition to the previous boundary conditions we should impose that the velocity field, the stress tensor of both fluids, and the fluid/fluid interface are periodic functions in the axial direction with period the length of the computational domain, $N\hat{L}$. It has been found that the length of the computational domain can greatly affect the stability and dynamics of the two-phase flow (Kouris & Tsamopoulos 2001*a*) depending on the wavelength of the critical disturbance, which in turn depends on the values of the dimensionless numbers. More specifically, if the length of the actual critical mode were larger than the computational domain, then the associated steady state would appear to be stable. At this point it is worth noting that the length of the domain and the effect of the imposed boundary conditions in the axial direction has never been taken into account, see for example Lahbabi & Chang (1986); Guzman

& Amon (1996); Amon, Guzman & Morel (1996). In contrast, here special care has been taken with this effect by increasing the length of the domain and considering as many geometrical constricted units as computationally possible. Although we have not completely eliminated this effect, we have reduced it considerably as is shown in our results.

(iii) Finally, additional overall conditions must be set in order to complete the problem formulation. It was found that, when the volumetric flow rates of both phases were set separately, unrealistic and non-converging results were obtained. On the other hand, setting the volume of the core fluid as well as either total volumetric flow rate of both phases or the pressure drop to a constant gave realistic results. Usually, we prefer to impose the former condition and *a posteriori* compute the pressure drop, checking in this way the convergence of the steady solutions.

Next, the above equations (2.4)–(2.6) together with the boundary conditions (2.9)–(2.12) are made dimensionless. The radial coordinate has been made dimensionless by using the maximum radius of the tube $\hat{R}_{max}$ and the axial coordinate by using the length $\hat{L}/(2\pi)$. The characteristic velocity in the axial direction, $\hat{W}_o$, is chosen so that the total volumetric flow rate of both fluids equals unity, i.e.

$$\hat{W}_o = \left(\int_0^{\hat{R}_1} \hat{r}\hat{W}_1 \, \mathrm{d}\hat{r} + \int_{\hat{R}_1}^{\hat{R}_2} \hat{r}\hat{W}_2 \, \mathrm{d}\hat{r} \right) \Big/ \hat{R}_{max}^2. \tag{2.13}$$

The characteristic velocity in the radial direction, $\hat{U}_o$, is related to $\hat{W}_o$ by

$$\hat{U}_o = \frac{2\pi\hat{R}_{max}}{\hat{L}} \hat{W}_o. \tag{2.14}$$

The pressure as well as the components of the stress tensor of each fluid are made dimensionless by dividing them with $\hat{\rho}_1 \hat{W}_o^2$, while time is scaled with $\hat{L}/(2\pi\hat{W}_o)$. Using the streamfunction–vorticity foumulation, the characteristic value of the streamfunction is $\hat{W}_o \hat{R}_{max}^2$, while the characteristic value of the vorticity is $\hat{W}_o / \hat{R}_{max}$. After introducing the above scales into (2.1)–(2.12), the following six dimensionless numbers appear: the constriction ratio $\alpha = \hat{R}_{min}/\hat{R}_{max}$, the aspect ratio $\Lambda = 2\pi\hat{R}_{max}/L$, the viscosity ratio $\mu = \hat{\mu}_2/\hat{\mu}_1$, the density ratio $\rho = \hat{\rho}_2/\hat{\rho}_1$, the Reynolds number $Re = (\Lambda\hat{W}_o\hat{R}_{max}\,\hat{\rho}_1)/\hat{\mu}_1$ and the inverse Weber number $W = \hat{T}/(\hat{\rho}_1\hat{W}_o^2\,\hat{R}_{max})$. The ratio of the volume of the core fluid to that of the tube, V_1/V_T, does not arise in the above set of equations, but must be fixed in order to have a well-posed problem.

3. Transformations

The introduction of the streamfunction, Ψ_i, and the definition of the vorticity, Ω_i, for each fluid, i, permit us to exactly satisfy the mass balances, (2.4), and by cross-differentiation of (2.5) to eliminate the pressure terms. As a result, the number of total unknowns and the computational cost are reduced. Equations (2.3)–(2.12) are transformed using the following relationships:

$$U_i = -\frac{1}{r}\frac{\partial\Psi_i}{\partial z}, \quad W_i = -\frac{1}{r}\frac{\partial\Psi_i}{\partial r} \tag{3.1}$$

$$\Omega_i = \frac{\partial W_i}{\partial r} - \frac{\partial U_i}{\partial z}. \tag{3.2}$$

The resulting dimensionless equations are the following:

$$r\Psi_{i,rr} - \Psi_{i,r} + \Lambda^2 r\,\Psi_{i,zz} - r^2\Omega_i = 0, \tag{3.3}$$

$$\rho_i\,Re\,r^2\Omega_{i,t} + (\rho_i\,Re\,\Psi_{i,z} + \mu_i)(\Omega_i - r\Omega_{i,r}) + \rho_i\,Re\,r\,\Psi_{i,r}\,\Omega_{i,z} - \mu_i\,r^2(\Omega_{i,rr} + \Lambda^2\Omega_{i,zz}) = 0, \tag{3.4}$$

$$R_1\,R_{1,t} + R_{1,z}\,\Psi_{1,r} + \Psi_{1,z} = 0, \tag{3.5}$$

where $(\mu_1, \rho_1) = (1, 1)$ and $(\mu_2, \rho_2) = (\mu, \rho)$ while the subscripts (r, z, t) imply differentiation with respect to radial and axial distance and time, respectively. The boundary conditions (2.9)–(2.11) along with the condition of axial symmetry of the velocity field ($U_1 = \partial W_1/\partial r = 0$ on $r = 0$) are expressed in terms of the streamfunction and vorticity and they become

$$\Psi_1 = -1, \quad \Psi_{1,r} = \Omega_1 = 0 \quad \text{on} \quad r = 0, \tag{3.6}$$

$$\Psi_1 - \Psi_2 = \Psi_{1,r} - \Psi_{2,r} = 0 \quad \text{on} \quad r = R_1(z,t), \tag{3.7}$$

$$\Psi_2 = \Psi_{2,r} = 0 \quad \text{on} \quad r = R_2(z). \tag{3.8}$$

The constant values of the streamfunction at $r = 0$ and $R_2(z)$ are chosen so that the total dimensionless volumetric flow rate equals unity. The stress balance given in (2.12) involves the pressure term. For that reason we need to differentiate this equation with respect to the axial distance, employing the following identity:

$$\frac{\partial}{\partial z}((\cdot)\big|_{r=R_1(z,t)}) \equiv \left.\frac{\partial(\cdot)}{\partial z}\right|_{r=R_1(z,t)} + R_{1,z}\left.\frac{\partial(\cdot)}{\partial r}\right|_{r=R_1(z,t)}. \tag{3.9}$$

In this way the resulting equation involves only the derivatives of pressure with respect to the axial and radial direction respectively, which can be easily eliminated by using (2.5). The final equations of the normal and tangential force balances are not given explicitly for brevity. We only note that an additional dimensionless number arises in the normal force balance, the inverse Weber number. Before proceeding further it is worth noting the way that we have satisfied implicitly some of the boundary conditions at the axis of symmetry as well as at the solid surface by introducing the following transformations:

in fluid 1:

$$\Psi_1 = r^2\,\psi_1 - 1; \tag{3.10}$$

in fluid 2:

$$\Psi_2 = (r - R_2)\psi_2. \tag{3.11}$$

Using the transformations (3.10)–(3.11), the conditions (3.6)–(3.8) reduce to

$$\psi_{1,r} = 0 \quad \text{on} \quad r = 0, \tag{3.12}$$

$$\psi_2 = 0 \quad \text{on} \quad r = R_2(z), \tag{3.13}$$

$$R_1^2\,\psi_1 - (R_1 - R_2)\psi_2 = 1,$$
$$2R_1\psi_1 - \psi_2 + R_1^2\,\psi_{1,r} - (R_1 - R_2)\psi_{2,r} = 0 \quad \text{on} \quad r = R_1(z,t). \tag{3.14}$$

The benefit of this is that we only have to impose four boundary conditions, (3.12)–(3.14), instead of seven, (3.6)–(3.8), as the other three are identically satisfied.

The fluid/fluid interfacial conditions must be applied on a moving and *a priori*

unknown boundary. In order to correctly and efficiently impose them, we employ the following non-orthogonal, body-fitted coordinate transformation $(r, z, t) \rightarrow (x_1, x_2, \tau)$ which maps it onto the fixed $x_1 = -1$ plane for both fluids:

fluid 1:

$$x_1 = 1 - 2\frac{r}{R_1(\theta, z, t)}, \quad x_2 = \frac{z}{N}, \quad \tau = t; \tag{3.15}$$

fluid 2:

$$x_1 = -1 + 2\frac{r - R_1(\theta, z, t)}{R_2(z) - R_1(\theta, z, t)}, \quad x_2 = \frac{z}{N}, \quad \tau = t. \tag{3.16}$$

This normalization transforms the boundaries of the region that each fluid occupies to coordinate lines in the new, transformed space. The bounds of the new independent variables are

$$-1 \leqslant x_1 \leqslant 1, \quad 0 \leqslant x_2 \leqslant 2\pi, \quad \tau \geqslant 0. \tag{3.17}$$

4. Steady solution and stability analysis

The steady version of the above equations results by setting $\partial(\cdot)/\partial t = 0$. In a periodically constricted tube the base solution cannot be derived analytically; it must be calculated numerically using the Newton–Raphson method. Owing to the fairly complicated form of the equations and to avoid additional matrix manipulations, the Jacobian matrix is formed numerically and its entries $(J_{i,j})$ are defined and then approximated using the following expressions:

$$J_{i,j} = \frac{\partial R_i}{\partial a_j} \approx \frac{R_i(a_j + \Delta a_j) - R_i(a_j)}{\Delta a_j}, \quad \Delta a_j = 0.5 \times 10^{-8} \max(1, |a_j|), \tag{4.1}$$

where R_i is the residual equation that corresponds to the ith unknown while a_j is the value of the jth unknown. A direct solver for linear equations was used which employs LU decomposition. Closer to convergence the Jacobian matrix was not updated in order to reduce the computational cost. Finally, in some cases, especially with a large Reynolds number or small viscosity or small constriction ratio, it was found unavoidable to use continuation in the parameter space in order to compute the basic flow.

After computing the steady axisymmetric solution, denoted by the subscript s, its temporal stability is examined. To this end, the steady solution is perturbed and the perturbation variables are denoted by the subscript p. Using the following expansion:

$$\begin{bmatrix} \psi_i(x_1, x_2, \tau) \\ \Omega_i(x_1, x_2, \tau) \\ R_1(x_2, \tau) \end{bmatrix} = \begin{bmatrix} \psi_{i,s}(x_1, x_2) \\ \Omega_{i,s}(x_1, x_2) \\ R_{1,s}(x_2) \end{bmatrix} + \delta \begin{bmatrix} \psi_{i,p}(x_1, x_2) \\ \Omega_{i,p}(x_1, x_2) \\ R_{1,p}(x_2) \end{bmatrix} \exp(\sigma\tau) \tag{4.2}$$

and omitting terms of order higher than δ, where δ is the perturbation parameter, one can obtain a generalized eigenvalue problem of the form: $\boldsymbol{J}\boldsymbol{x} = \sigma \boldsymbol{M}\boldsymbol{x}$ where $\boldsymbol{J}$ is the Jacobian and $\boldsymbol{M}$ the mass matrix, respectively. In (4.2) σ is the temporal eigenvalue of the linearized equations. The real part of the eigenvalue, denoted by σ_R, corresponds to the growth rate of the disturbance while the imaginary part, denoted by σ_I, corresponds to the temporal oscillation frequency. When the real parts of all the eigenvalues are negative the steady state is said to be stable to infinitesimal disturbances and the corresponding steady-state solution is physically realizable, while when there is at least one eigenvalue with positive real part the steady state is classified

as unstable. In the limiting case where all the eigenvalues have negative real parts except for some whose real parts equal zero, then this steady state is said to be neutrally stable with respect to these disturbances. The Jacobian matrix is in general invertible, except when an eigenvalue is identically zero. On the other hand, the mass matrix is always non-invertible because equation (3.3), in addition to certain boundary conditions, does not involve time derivatives. In order to reduce the computational cost of storing two square matrices and solving a generalized eigenvalue problem we transform it first to the equivalent ordinary eigenvalue problem:

$$(\boldsymbol{J}^{-1}\,\boldsymbol{M})\boldsymbol{x} = \frac{\sigma^*}{\sqrt{\sigma_R^2 + \sigma_I^2}}\boldsymbol{x}, \tag{4.3}$$

where * denotes complex conjugate. Clearly when the real part of the most dangerous eigenvalue of the original problem changes sign, so does the most dangerous one of the transformed problem, while its eigenvector remains unchanged. This eigenvalue problem is solved using Arnoldi's method, which locates only the eigenvalues of interest, i.e. those with the smallest real part (Saad 1980; Christodoulou & Scriven 1988; Anturkar, Papanastasiou & Wilkes 1991; Huang & Joseph 1995). According to it, given the matrix $\boldsymbol{A}(n \times n)$ another matrix $\boldsymbol{V}_m(m \times n)$ is created with columns the $m(\ll n)$ linearly independent vectors, $\boldsymbol{v}_1, \boldsymbol{A}\boldsymbol{v}_1, \ldots, \boldsymbol{A}^{m-1}\boldsymbol{v}_1$ which are made orthonormal to each other using the following iterative sequence:

$$\hat{\boldsymbol{v}}_{j+1} = \boldsymbol{A}\boldsymbol{v}_j - \sum_{i=1}^{j} h_{i,j}\,\boldsymbol{v}_j; \quad h_{i,j} = (\boldsymbol{v}_i, \boldsymbol{A}\boldsymbol{v}_j); \quad \boldsymbol{v}_{j+1} = \hat{\boldsymbol{v}}_{j+1}/h_{j+i,j}. \tag{4.4}$$

The coefficients $\boldsymbol{h}_{ij}$ form an upper Hessenberg matrix, $\boldsymbol{H}$, the eigenvalues of which approximate the eigenvalues of the original matrix. For implementing the Arnoldi algorithm we have used the commercially available software developed by Lehoucq & Scott (1996). This code is capable by default of computing the eigenvalues with the largest magnitude and not those with the smallest real part. We have observed that in cases where modes with long wavelengths are the most critical ones ($Re \ll 1$) then this software is capable of locating the most dangerous eigenvalues by computing only 10–20 out of the over 10^3 eigenvalues. However, in cases with $Re \gg 1$ the critical modes are characterized by short wavelength and large temporal frequencies and, as a result, the number of eigenvalues that need to be computed increases to, in some cases, above 300. In none of the cases examined have spurious eigenvalues been encountered.

It is worth noting here that, due to the periodic constrictions of the tube, the steady solution is inherently a two-dimensional one and, as result, we cannot study its stability by adopting the normal mode decomposition in the axial direction as in the case of the straight tube. In a straight tube the axial dependence of the eigenvectors is written in terms of decoupled Fourier modes of arbitrary wavenumber and, thus, a much simpler, one-dimensional eigenvalue problem needs to be solved in the radial direction. In the present case however, the eigenspectrum is disrupted by the imposed periodic boundary conditions, hence the wavelength of any disturbance can only be an integer multiple of the length of the geometry. This observation is valid not only in CAF, but also in single-phase flow studied by Lahbabi & Chang (1986). Clearly, knowledge of the axial dependence of the eigenvector not only would simplify the numerical solution of the problem, but also it would give us the ability to examine thoroughly the stability of CAF in a large series of undulations. However, due to computer limitations their number must remain finite and we take every care in order

to minimize the effects of the periodic boundary conditions by increasing it as much as possible.

5. Energy analysis

If a steady solution is unstable, the amplitude (and the energy) of initially small disturbances will grow in time. Although it is clear that this energy is being supplied by the primary flow, where it is directed and the mechanism by which this takes place are not clear in general. In a two-phase flow a growing disturbance may be due to increasing energy in the bulk of either fluid, similar to the mechanisms in a single-phase flow, giving rise usually to unstable modes of short wavelength. Alternatively, a growing disturbance may be due to increasing energy at the interface due to capillary forces or viscosity stratification or from a combination of the above sources. Examining the energy associated with each one may lead to identification of the predominant instability mechanism, see Hooper & Boyd (1983), Hu & Joseph (1989) and Boomkamp & Miesen (1997). Owing to the mapping, (3.15)–(3.16), the free boundary problem is transformed into an equivalent one with fixed boundaries and the effect of the interface is reflected by the many additional terms that arise in the governing equations due to the transformation. Although this transformation is essential to correctly impose both the interfacial conditions and the conditions at the wavy solid wall, given the adopted method of solution, it is much more efficient to use the domain perturbation technique (Joseph 1973) to calculate the various energy terms in the linearized energy equation. To this end, we transform the computed eigenvectors and their derivatives back to the ones that we would have obtained had we adopted the domain perturbation technique. Some details of this complicated transformation are given in Kouris & Tsamopoulos (2000).

The starting point of the energy calculation is the axisymmetric linearized equations of motion multiplied by the complex conjugate of the corresponding eigenvector and integrated over the length of the tube and the thickness of each fluid. Upon application of the divergence theorem we obtain the following energy terms:

(*a*) The rate of change of the kinetic energy of the distriburbance for each fluid (E_i) is defined by the following integral:

$$E_i = \rho_i \sigma_R \int_{V_i} \left(\Lambda^2 \left(U_{i,p}^{R^2} + U_{i,p}^{I^2} \right) + \left(W_{i,p}^{R^2} + W_{i,p}^{I^2} \right) \right) \mathrm{d}V, \tag{5.1}$$

where $\mathrm{d}V = r\,\mathrm{d}r\,\mathrm{d}z$ and V_i corresponds to the volume that each fluid occupies in the base state, while the subscripts i and p indicate the ith fluid and the perturbation solution, respectively and the superscripts R and I refer to the real and the imaginary part of the eigenvector. Clearly this integral is non-negative and the sign of the real part of the eigenvalue determines the sign of the rate of change of the kinetic energy of each fluid. Therefore when σ_R is positive the disturbance kinetic energy increases exponentially in time implying an unstable steady state.

(*b*) The rate of viscous dissipation of the perturbed flow of each fluid (D_i) is defined as

$$D_i = -\int_{V_i} \left(\tau_{i,p,rz}^{R^2} + \tau_{i,p,rz}^{I^2} + \tfrac{1}{2} \left(\tau_{i,p,rr}^{R^2} + \tau_{i,p,rr}^{I^2} + \tau_{i,p,\theta\theta}^{R^2} + \tau_{i,p,\theta\theta}^{I^2} \right) \right) \mathrm{d}V, \tag{5.2}$$

where $\tau_{i,p,jk}$ denotes the jkth component of the dimensionless disturbance stress tensor $\boldsymbol{\tau}_{i,p}$ of the ith fluid. Clearly the sign of this term is negative and, as a result, viscous dissipation always stabilizes the flow.

(*c*) The rate at which the Reynolds stress is transferring energy between the primary and the disturbed flow (RS_i) in the bulk of both fluids is defined as

$$RS_i = -\rho_i \int_{V_i} \begin{pmatrix} \Lambda^2 U^R_{i,p}\left(U^R_{i,p}\dfrac{\partial U_{i,s}}{\partial r} + U_{i,s}\dfrac{\partial U^R_{i,p}}{\partial r} + W^R_{i,p}\dfrac{\partial U_{i,s}}{\partial z} + W_{i,s}\dfrac{\partial U^R_{i,p}}{\partial z}\right) \\ +\Lambda^2 U^I_{i,p}\left(U^I_{i,p}\dfrac{\partial U_{i,s}}{\partial r} + U_{i,s}\dfrac{\partial U^I_{i,p}}{\partial r} + W^I_{i,p}\dfrac{\partial U_{i,s}}{\partial z} + W_{i,s}\dfrac{\partial U^I_{i,p}}{\partial z}\right) \\ +W^R_{i,p}\left(U^R_{i,p}\dfrac{\partial W_{i,s}}{\partial r} + U_{i,s}\dfrac{\partial W^R_{i,p}}{\partial r} + W^R_{i,p}\dfrac{\partial W_{i,s}}{\partial z} + W_{i,s}\dfrac{\partial W^R_{i,p}}{\partial z}\right) \\ +W^I_{i,p}\left(U^I_{i,p}\dfrac{\partial W_{i,s}}{\partial r} + U_{i,s}\dfrac{\partial W^I_{i,p}}{\partial r} + W^I_{i,p}\dfrac{\partial W_{i,s}}{\partial z} + W_{i,s}\dfrac{\partial W^I_{i,p}}{\partial z}\right) \end{pmatrix} \mathrm{d}V. \tag{5.3}$$

(*d*) The rate at which work is done by the velocity and stress disturbances in the direction normal (B_N) and tangent (B_T) to the interface are defined as

$$B_N = \int_0^{2\pi N} \frac{\partial R_{1,s}}{\partial z} \begin{pmatrix} \left(U^R_{1,p} - \Lambda\dfrac{\partial R_{1,s}}{\partial z}W^R_{1,p}\right)\left(-\tilde{p}^R_{1,p} + \boldsymbol{\tau}^R_{1,p}\cdot\boldsymbol{n}\right) \\ -\left(U^R_{2,p} - \Lambda\dfrac{\partial R_{1,s}}{\partial z}W^R_{2,p}\right)\left(-\tilde{p}^R_{2,p} + \boldsymbol{\tau}^R_{2,p}\cdot\boldsymbol{n}\right) \\ +\left(U^I_{1,p} - \Lambda\dfrac{\partial R_{1,s}}{\partial z}W^I_{1,p}\right)\left(-\tilde{p}^I_{1,p} + \boldsymbol{\tau}^I_{1,p}\cdot\boldsymbol{n}\right) \\ -\left(U^I_{2,p} - \Lambda\dfrac{\partial R_{1,s}}{\partial z}W^I_{2,p}\right)\left(-\tilde{p}^I_{2,p} + \boldsymbol{\tau}^I_{2,p}\cdot\boldsymbol{n}\right) \end{pmatrix} \cdot\boldsymbol{n}\,\mathrm{d}z, \tag{5.4}$$

$$B_T = \int_0^{2\pi N} \frac{\partial R_{1,s}}{\partial z} \begin{pmatrix} \left(\Lambda\dfrac{\partial R_{1,s}}{\partial z}U^R_{1,p} + W^R_{1,p}\right)\boldsymbol{\tau}^R_{1,p}\cdot\boldsymbol{n} \\ -\left(\Lambda\dfrac{\partial R_{1,s}}{\partial z}U^R_{2,p} + W^R_{2,p}\right)\boldsymbol{\tau}^R_{2,p}\cdot\boldsymbol{n} \\ +\left(\Lambda\dfrac{\partial R_{1,s}}{\partial z}U^I_{1,p} + W^I_{1,p}\right)\boldsymbol{\tau}^I_{1,p}\cdot\boldsymbol{n} \\ -\left(\Lambda\dfrac{\partial R_{1,s}}{\partial z}U^I_{2,p} + W^I_{2,p}\right)\boldsymbol{\tau}^I_{2,p}\cdot\boldsymbol{n} \end{pmatrix} \cdot\boldsymbol{t}\,\mathrm{d}z, \tag{5.5}$$

where $\boldsymbol{n}$ and $\boldsymbol{t}$ are the unit vectors normal and tangent to the steady fluid/fluid interface. It is worth noting that the boundary term normal to the interface arising from the energy equation after applying the divergence theorem involves the disturbed pressures of both fluids. Since we have eliminated the pressure terms from the linearized equations of motion of both fluids while using the streamfunction–vorticity formulation, we have to compute the pressure terms after having computed the eigenvector by solving a second-order partial differential equation in both spatial directions. Furthermore, the pressure terms arising in the energy term B_N which has been attributed to the normal stress condition, see (5.4), cannot be directly eliminated using the interfacial force balances. As a result, B_N appears to depend not only on the surface tension parameter as in the case of the straight tube geometry but also on the viscosity ratio and the Reynolds number. However, by setting the surface tension equal to zero or the viscosity ratio equal to unity we have found that the terms B_N and B_T become zero correspondingly for all values of Re, indicating a direct effect

on W and μ on these energy terms. Hence, we prefer to compute the B_N term taking advantage of the fact that the sum of all the energy terms equals zero. The sign of the last three energy terms can be positive or negative and, as a result, it is not possible to determine *a priori* whether they stabilize or destabilize the system, since their effect depends on the values of the dimensionless numbers. Each one of the above energy terms has been normalized by the sum of the dissipative terms following the idea by Hu & Joseph (1989). Therefore, in all the cases where values of the energy terms are given, the sum of the dissipative terms of both fluids equals unity.

6. Numerical implementation

In order to solve both the steady and the eigenvalue problem in the streamfunction–vorticity formulation we use a pseudo-spectral method. This method is preferred because of its exponential rate of convergence with mesh refinement (Gottlieb & Orszag 1977; Canuto *et al.* 1988). We approximate every dependent valuable by Chebyshev polynomials in the x_1-direction and Fourier modes in the x_2-direction. The grid points in the x_1-direction are given by $x_{1k} = \cos(\pi(k-1)/(K-1))$, $1 \leqslant k \leqslant K$, while the grid points in the x_2-direction are taken to be equidistant $x_{2m} = (2\pi(m-1)/M)$, $1 \leqslant m \leqslant M$, where $(M-1)/2$ is the highest number of Fourier modes which has been used. The division by 2 is due to the fact that every Fourier mode includes both a sine and a cosine component while the -1 is due to the single (first) constant mode. So, every dependent variable is approximated as a sum of products of Chebyshev polynomials, C_i, and Fourier modes, F_j, i.e.

$$f(x_1, x_2) = \sum_{i=1}^{K} \sum_{j=1}^{M} a_{ij}\, C_i(x_1)\, F_j(x_2). \tag{6.1}$$

The derivative of each function with respect to every variable is evaluated by differentiating term by term its spectral expansion and, thus, by forming the 'derivative' matrices. Finally the unknowns of the summation (6.1), a_{ij}, equal the number of collocation points and they are evaluated by satisfying the differential equations at these points. By using M and K unknowns in the axial and radial direction, respectively, the total number of unknowns is $4MK + M$ for both the steady and the eigenvalue problem.

In order to evaluate the various energy terms, the region that each fluid occupies is divided into quadrilateral finite elements and then each variable is approximated by linear Lagrangian basis functions in each direction. The Galerkin-weighted residuals are formed and the resulting two-dimensional integrals are evaluated by using four Gauss points and the one-dimensional ones by using two. Convergence of the values of the energy terms with increasing the number of the elements is achieved in this case too.

7. Comparison with literature results

The most sensitive among our calculations are those that involve computation of the eigenvalues. Because of this, our results are compared carefully to literature results next. By setting the constriction ratio to unity ($\alpha = 1$) the straight tube geometry is recovered. Although this is just a limiting case, there are many reported results that can be used to check the accuracy of our calculations. First, the case of an unbounded and infinitely long jet with high viscosity is examined using the following values of the

v	x^{Ch}	Exact (σ_R^{Ch})	This work (σ_R)
1	0.2	0.16000	0.15996
2	0.4	0.14000	0.13997
3	0.6	0.10660	0.10657
4	0.8	0.05984	0.05985
5	1.0	0.00000	0.00000

TABLE 1. Comparison of the growth rates from the present analysis with those reported by Chandrasekhar (1981) for the instability of a high-viscosity and infinte jet.

dimensionless numbers: $\mu = 0.5 \times 10^{-5}$, $\rho = 0$, $Re = 10^{-3}$, $W = 1$, $\Lambda = 0.2\pi$, $R_1 = \pi^{-1}$. We assign a very small value to the Reynolds number ($Re \ll 1$) so that the jet is very viscous. Furthermore, we set the viscosity ratio such that both $\mu \ll 1$ and $\mu/Re \ll 1$, and the density ratio to zero. In this way the flow of the jet is decoupled from that of the surrounding medium, since the latter exerts no force on the former through the tangential force balance ($\mu \ll 1$). Also, in the momentum balance of the annular fluid, on one hand the inertia terms are multiplied by zero ($\rho = 0$) and, on the other hand, the viscous terms are subdominant to the corresponding ones of the jet ($\mu/Re \ll 1$). Finally, a relatively small value of the inverse Weber number is used so that, among the various terms appearing in the normal force balance, pressure forces and viscous stresses (both arising from the jet) dominate. By using the following relation we recover the eigenvalues of the most unstable mode, which indeed correspond to the viscous jet instability reported by Chandrasekhar (1981):

$$x^{Ch} = v\Lambda R_1, \quad \sigma_R^{Ch} = \sigma_R \Lambda^2 R_1 \frac{W}{Re}. \tag{7.1}$$

The superscript Ch indicates variables used by Chandrasekhar (1981) and v is the axial wavenumber. The excellent agreement between the two sets of results can be seen in table 1, where only the growth rates are reported. Results from the same table verify that in this case the growth rate decreases monotonically with increasing the wavenumber and that the most dangerous wave is the longest one.

In order to recover the Rayleigh stability limit (Chandrasekhar 1981) of an inviscid and unbounded jet we use the following values of the dimensionless numbers: $\mu = 0.5 \times 10^{-5}$, $\rho = 0$, $Re = 10^2$, $W = 2 \times 10^2$, $\Lambda = 0.2\pi$, $R_1 = \pi^{-1}$. We have chosen values for the viscosity ratio and the Reynolds number such that $\mu \ll 1$ and $\mu/Re \ll 1$. Furthermore, now we have used larger values for the Reynolds and the inverse Weber numbers so that the force balance in the normal stress condition is predominantly between pressure and capillary forces. The relation between the variables employed here and those employed by Rayleigh is

$$x^{Ra} = v\Lambda R_1, \quad \sigma_R^{Ra} = \sigma_R \Lambda \sqrt{\frac{R_1^3}{W}}. \tag{7.2}$$

Using (7.2) we obtain the growth rates that are reported in table 2. Obviously the agreement is again excellent, while it can be clearly seen that now the most dangerous wave is not the longest one as the growth rate is maximized for about $x^{Ra} = 0.6$. It is well known that the wavelength for which the growth rate of an inviscid jet is maximized is $x^{Ra} = 0.697$, but due to the periodic boundary conditions that we have imposed, we cannot capture this value unless the length of the computational

v	x^{Ra}	Exact (σ_R^{Ra})	This work (σ_R)
1	0.2	0.1382	0.1382
2	0.4	0.2567	0.2566
3	0.6	0.3321	0.3319
4	0.8	0.3269	0.3266
5	1.0	0.0000	0.0002

TABLE 2. Comparison of the growth rates from the present analysis with those reported using the inviscid analysis by Rayleigh.

Case	Eigenvalues reported by Hu & Joseph (1989)	This work (streamfunction–vorticity)
1	$0.020874 \pm 0.38614 \cdot i$	$0.020978 \pm 0.38485 \cdot i$
2	$0.004137 \pm 0.66934 \cdot i$	$0.004147 \pm 0.66939 \cdot i$

TABLE 3. Comparison with the results reported by Hu & Joseph (1989) for CAF in a straight tube.

domain is an integer multiple of it. Another observation that we can make is that for wavelength $x^{Ra} = 0$ the growth rate goes to zero as it should.

In the second column of table 3, we present eigenvalues of CAF in a straight tube as computed by Hu & Joseph (1989) and reported in their table 1, for axisymmetric modes. In the next column, we present the eigenvalues computed by using our code based on the streamfunction–vorticity formultion. The values of the dimensionless numbers $(J^*, \eta, m, \zeta, k, \beta, R^{HJ})$ that Hu & Joseph (1989) report for these two cases are the following: Case 1: $(1000, 0.9, 0.05, 1, 0, 5, 500)$, Case 2: $(0, 0.7, 0.5, 1, 0, 10, 37.78)$.

Their dimensionless numbers are related to ours as follows:

$$\left.\begin{aligned} &\mu = m, \quad \rho = \zeta, \quad \frac{V_1}{V_T} = \eta^2, \quad \Lambda = \beta, \quad A = 1 - m(1-\eta^2), \\ &Re = \frac{R^{HJ}\beta}{4A}(\eta^4(1-m) + 2(1-\eta^2) - (1+2A\eta^2)), \\ &W = J^* \left(\frac{4A}{R^{HJ}\left(\eta^4(1-m) + 2(1-\eta^2) - (1-2A\eta^2)\right)} \right)^2 . \end{aligned}\right\} \tag{7.3}$$

From the comparison of our results with those obtained by Hu & Joseph (1989) we conclude that there is complete agreement between the results already reported in the literature and ours.

Moreover, we have examined the validity of the analytically computed eigenvalues for CAF in a straight tube for small Renolds number ($\mu_i/Re \gg 1$) and large surface tension ($W \geqslant O(1/Re)$). These were derived in Kouris & Tsamopoulos (2000*a*) who used lubrication theory and, as a result, their analysis is accurate only for very long waves. According to them, the real and imaginary parts of the eigenvalues are

$$\left.\begin{aligned} \sigma_R &= -\frac{v^2\, Re\, W\left(1 - v^2\, \Lambda^2 R_1^2\right) R_1}{4\mu} \\ &\quad \times \left(\ln(R_1) + (1 - R_1^2)\frac{1 + (\mu-1)R_1^2 - 0.25\mu(1+R_1^2)}{1 + (\mu-1)R_1^4} \right), \\ \sigma_I &= \pm 4v(R_1^2 - 1)\frac{1 + (\mu-1)R_1^2}{(1 + (\mu-1)R_1^4)^2}. \end{aligned}\right\} \tag{7.4}$$

v	Lubrication approximation $\sigma_R \pm \sigma_I$ I	Complete equations $\sigma_R \pm \sigma_I$ i
1	0.032038 ± 2.79709·I	0.031337 ± 2.81565·i
2	0.102522 ± 5.59417·I	0.093819 ± 5.65902·i
3	0.134560 ± 8.39126·I	0.110733 ± 8.59168·i
4	0.000000 ± 11.1883·I	0.000221 ± 11.6117·i
5	-0.480570 ± 13.9854·I	-0.289801 ± 14.7075·i

TABLE 4. Comparison with the analytical (long-wave) solution for the following values of the dimensionless numbers $(\mu, Re, W, R_1, \Lambda) = (0.5, 0.01, 100, 0.5, 0.5)$.

Equation (7.4) is different from that obtained by Preziosi *et al.* (1989), since the eigenvalues depend on the axial wavenumber, v, as well. It is also different from the characteristic equation reported by Papageorgiou *et al.* (1990) since it includes the dependence on the thickness of the core fluid, R_1. In table 4 we compare the computed eigenvalues of the complete Navier–Stokes equations with the predicted ones using equation (7.4). The difference between the analytical solution and the results obtained numerically by solving the complete equations for the longest mode is about 2% for the real part of the eigenvalue and much smaller for the imaginary part. This error increases with increasing wavenumber and becomes approximately 9% for $v = 2$ and 20% for $v = 3$ for the respective real parts. This deviation of the results with increasing the wavenumber is due to the fact that the lubrication approximation is a long-wave expansion and as a result it can only accommodate waves very long compared to the radius of the tube.

Finally, we have examined the accuracy of our energy calculations in the case of CAF in a straight tube as can be seen in table 5. The energy results in this table are compared to those by Hu & Joseph (1989) and are obtained by using values for the dimensionless numbers that correspond to the conditions in the experiments by Aul & Olbricht (1990). By using again the dimensionless numbers which Hu & Joseph (1989) report in their paper (see their table 4) and using (7.3) to convert them to ours, we obtain very similar results. Both sets of results in this table predict that with increasing *Re*, the dominant mechanism of instability switches from one due to capillarity (B_N is the largest term) to one due to the viscosity stratification (B_T is the largest term), a type of instability which can be thought of as the viscous analogue of Kelvin–Helmholtz instability. The Reynolds stresses in the bulk of both fluids remain insignificant irrespective of the Reynolds number.

In order to check the accuracy of our numerical scheme in the case of a constricted tube we reproduce results reported by Lahbabi & Chang (1986) for single-phase flow. They have computed the friction factor for various Reynolds numbers, which range from the creeping flow limit to cases for which a pronounced separation region exists in the expanding portion of the tube. Their results correspond to the case of a tube with constriction ratio and aspect ratio $\alpha = 0.538$ and $\Lambda = 1.307$, respectively. In order to reproduce their results both the viscosity and the density ratio are set to unity ($\mu = \rho = 1$) as well as $W = 0$. These values are chosen in order to suppress the effects of viscosity and density stratification and surface tension. Excellent agreement of our results with theirs has been achieved for all values of Reynolds number, even when *Re* is as large as 264.

As encouraging as this comparison may be, it does not check the accuracy of either imposing the interfacial conditions or determining the stability of the flow. To

Case	Re^{HJ}	$RS_1 + RS_2$	B_N	B_T	$E_1 + E_2$
		Results reported by Hu & Joseph (1989)			
1	0.005	0.21×10^{-6}	0.6605	0.3393	0.2117×10^{-6}
2	0.01	0.41×10^{-6}	0.3264	0.6733	0.4173×10^{-6}
3	0.0277	0.55×10^{-6}	0.05934	0.9402	0.5816×10^{-6}
4	0.05	0.49×10^{-6}	0.01899	0.9805	0.6065×10^{-6}
5	0.1	0.16×10^{-6}	0.4819×10^{-2}	0.9946	0.6155×10^{-6}
		This work			
1	0.005	0.21×10^{-6}	0.6573	0.3427	0.210×10^{-6}
2	0.01	0.41×10^{-6}	0.3285	0.6715	0.417×10^{-6}
3	0.0277	0.55×10^{-6}	0.05803	0.9419	0.581×10^{-6}
4	0.05	0.49×10^{-6}	0.01954	0.9804	0.606×10^{-6}
5	0.1	0.16×10^{-6}	0.4014×10^{-2}	0.9960	0.353×10^{-4}

TABLE 5. Comparison with the energy results reported by Hu & Joseph (1989) for the experiments performed by Aul & Olbricht (1990) for CAF in a straight tube.

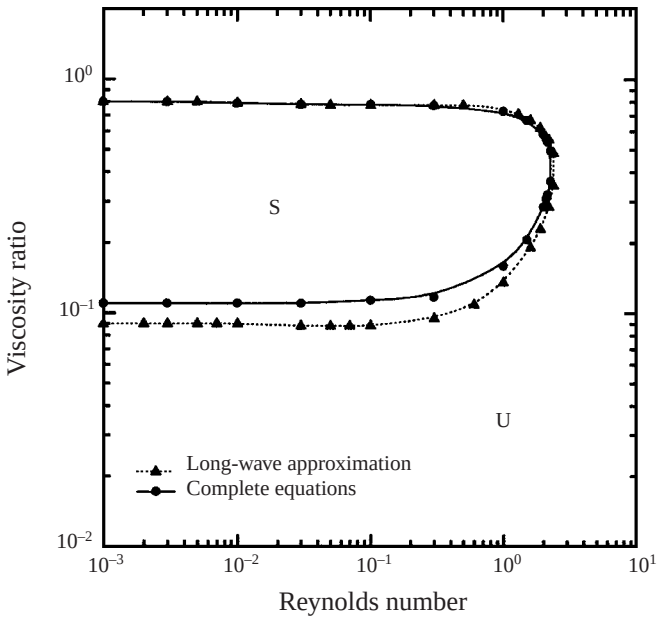

FIGURE 2. Marginal stability curves predicted by solving the complete equations and those obtained using lubrication theory. The dimensionless numbers for both curves are: $\rho = 1$, $W = 4$, $V_1/V_T = 0.75$, $\alpha = 0.8$, $\Lambda = 0.2\pi$, $N = 1$.

this end, next we compare our stability results with those obtained using a long-wave expansion for the case of two-phase flow in a constricted tube (Kouris & Tsamopoulos 2000). In figure 2 we give the critical curve that divides the plane of viscosity ratio versus Reynolds number into stable and unstable regions denoted by the letters S and U, respectively. The solid line is computed by solving the complete equations of motion of both fluids while the dotted line has been computed by solving the simplified lubrication equations. The values of the dimensionless numbers used

	Fourier modes	Chebyshev modes	Total unknowns	Leading eigenvalue
(*a*)	31	9	1147	$0.18147653 \times 10^{-5} \pm 0.97087095 \cdot \mathrm{i}$
	35	11	1575	$0.13636867 \times 10^{-5} \pm 0.97086901 \cdot \mathrm{i}$
	39	13	2067	$0.29235725 \times 10^{-5} \pm 0.97087758 \cdot \mathrm{i}$
	43	15	2623	$0.82232429 \times 10^{-5} \pm 0.97086104 \cdot \mathrm{i}$
(*b*)	61	9	2257	$0.18556984 \times 10^{-3} \pm 0.23834038 \cdot \mathrm{i}$
	65	11	2925	$0.41300999 \times 10^{-3} \pm 0.23649878 \cdot \mathrm{i}$
	69	13	3657	$0.77424919 \times 10^{-4} \pm 0.23677251 \cdot \mathrm{i}$

TABLE 6. Convergence of the leading eigenvalue at (*a*) small Reynolds number and small viscosity ratio in the following values of the dimensionless numbers: $(\mu, \rho, Re, W, V_1/V_T, \Lambda, \alpha, N) = (0.005, 1, 0.8646, 66.8867, 0.859, 0.25\pi, 0.8, 1)$ and (*b*) large Reynolds number and moderate viscosity ratio with the following values of the dimensionless numbers $(\mu, \rho, Re, W, V_1/V_T, \Lambda, \alpha, N) = (0.5165, 1, 87.5, 5, 0.859, 0.25\pi, 0.8, 5)$.

are the following: $\rho = 1$, $W = 4$, $\alpha = 0.8$, $V_1/V_T = 0.75$, $\Lambda = 0.2\pi$, $N = 1$. The agreement is satisfactory, as expected, since the small parameter of the lubrication approximation is taken to be less than unity $\Lambda/(2\pi) = 0.1 \ll 1$. It is noteworthy that in both formulations the most unstable mode is a long-wavelength one, because the computations were performed with a constant value of $W = O(1)$, thus validating the lubrication analysis.

Finally, in tables 6(*a*) and 6(*b*) one can see the convergence of the leading (most unstable) eigenvalue on increasing the total number of unknowns. These results correspond to two representative cases: the first to small Reynolds number and very small viscosity ratio; the second to large Reynolds number and moderate viscosity ratio. In both cases the effective Reynolds number of the outer fluid is large, leading to the formation of a vortex attached to the tube wall.

In spite of this, one can see that the imaginary part of the leading eigenmode converges to at least three significant digits while the total number of unknowns needed in order to get converged results increases with increasing the Reynolds number. Since the parameters are chosen so that we are very close to neutral stability, the real part of the eigenvalues is at least four orders of magnitude smaller than the imaginary part and, thus, it has already converged.

8. Steady-state results

For clearer presentation of the results the dimensionless length of each cell will be set to 1. Therefore, the axial distance henceforth will be denoted 'y' and it will vary between 0 and 1 for one cell, between 0 and 2 for two cells and so on, instead of between 0 and 2π in all these cases. Figure 3 shows the effect of the Reynolds number and the viscosity ratio (their respective values are given on the figure) on the steady-state shapes of the fluid/fluid interface in CAF in a constricted tube. The values of the rest of the dimensionless numbers remain constant. Clearly the interface follows the imposed symmetry between the entrance and the exit of the cell. In spite of the very small value of the viscosity ratio, $\mu = 0.005$, when $Re < 1$ the interface exhibits the symmetry at $y = 1/2$ expected for creeping flow conditions and closely follows the shape of the tube. Increasing fluid inertia to $Re = 1$, first shifts the interface to the direction of the flow both before and after the $y = 1/2$ plane, breaking the mid-plane symmetry. At even higher values of Re, e.g. $Re = 5$, the interface is forced abruptly

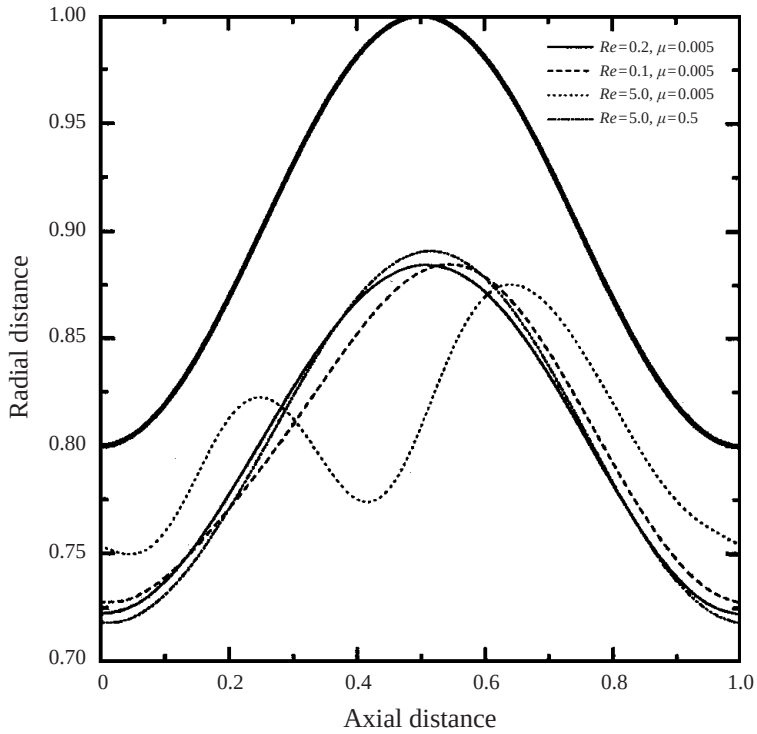

FIGURE 3. Effect of the Reynolds number and the viscosity ratio on the steady fluid/fluid interface, $\rho = 1$, $W = 10$, $V_1/V_T = 0.797$, $\alpha = 0.8$, $\Lambda = 0.25\pi$, $N = 1$. The thickest line indicates the location of the tube wall.

away from the tube wall before and around the $y = 1/2$ plane and it is uniformly pushed closer to the wall beyond the $y = 1/2$ plane. For mass conservation reasons, even near the entrance the interface approaches the tube wall. Thus, enough space is given to the outer fluid to separate and recirculate where the tube cross-section expands. Overall the interface becomes quite wavy and has a local minimum at axial distance close to the maximum of the radius of the tube wall and two local maxima around it. This distortion of the interafce increases when Re increases or the constriction ratio decreases from unity. The asymmetry of the interface and of the flow around $y = 1/2$ is gradually removed by increasing the viscosity ratio and disappears for $\mu = 0.5$. Comparing the two symmetric cases, the one with the larger viscosity ratio follows the variations of the tube wall more closely than the one with the smaller μ. In most cases with a more viscous fluid in the core, the annular film thickness is maximized (minimized) where the tube radius is maximized (minimized); the core fluid avoids entering the wall cavity.

Figure 4 shows the effect of the inverse Weber number, W, for values given on the figure. The values of $Re = 1, W = 10$ and $\mu = 0.005$ have been chosen so that a smooth interface is predicted according to the previous discussion. These parameter values generate an interface that is already not symmetric around the $y = 1/2$ plane, but it closely follows the shape of the tube. Increasing W increases the capillary force exerted on the curved interface from the annular to the core fluid owing to surface tension and, as a result, the interface follows the shape variation of the solid wall even less. At the highest value of W we examined, $W = 40$, the distortion of the interface increases further and it becomes wavy, allowing fluid recirculation to occur

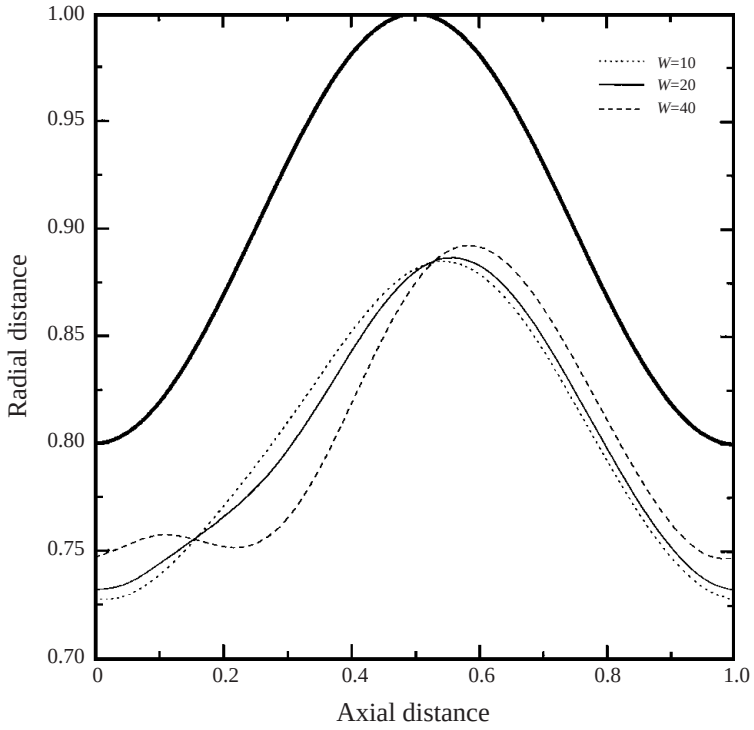

FIGURE 4. Effect of the inverse Weber number, W, on the steady fluid/fluid interface, $\mu = 0.005$, $\rho = 1$, $Re = 1$, $V_1/V_T = 0.797$, $\alpha = 0.8$, $\Lambda = 0.25\pi$, $N = 1$. The thickest indicates the location of the tube wall.

in the expanding portion of the tube in the region occupied by the annular fluid. Flow separation will arise there too; however, this distortion is not as large as the one caused by increasing *Re*.

Figure 5 shows the steady shape of the interface for different values of the viscosity and core volume ratios. Starting from the values $\mu = 0.005, V_1/V_T = 0.736$ it is observed that the interface exhibits the usual local minimum given the values of the rest of the parameters. Increasing the volume of the inner fluid decreases the space available to the outer one for its recirculation which, however, is not eliminated. On the contrary, its presence in a smaller volume makes the local extrema in the interface even more pronounced. Recirculation is eliminated and the interface again follows the surface of the tube on increasing the viscosity ratio.

The effect of the various parameters can also be seen in figure 6, where the steady streamlines in both fluids are depicted. The lower streamline gives the axis of symmetry, the upper one gives the tube wall and the thicker one with the arrows simultaneously gives the location of the common interface and the direction of the flow of the two liquids. The axis of the pipe, $r = 0$, as well as the solid surface of the tube, $r = R_2(z)$, correspond to streamlines of different constant values, -1 and 0, respectively, as in both surfaces the radial velocity of the fluids is identically zero. When $Re \ll 1$, the streamlines are symmetric around the mid-plane (figure 6*a*) as they should be in the creeping flow limit, in spite of the small values of μ which increases the effective *Re* of the annular fluid considerably. On physical grounds, the increase of fluid inertia is expected to produce separated flow regions. This does not

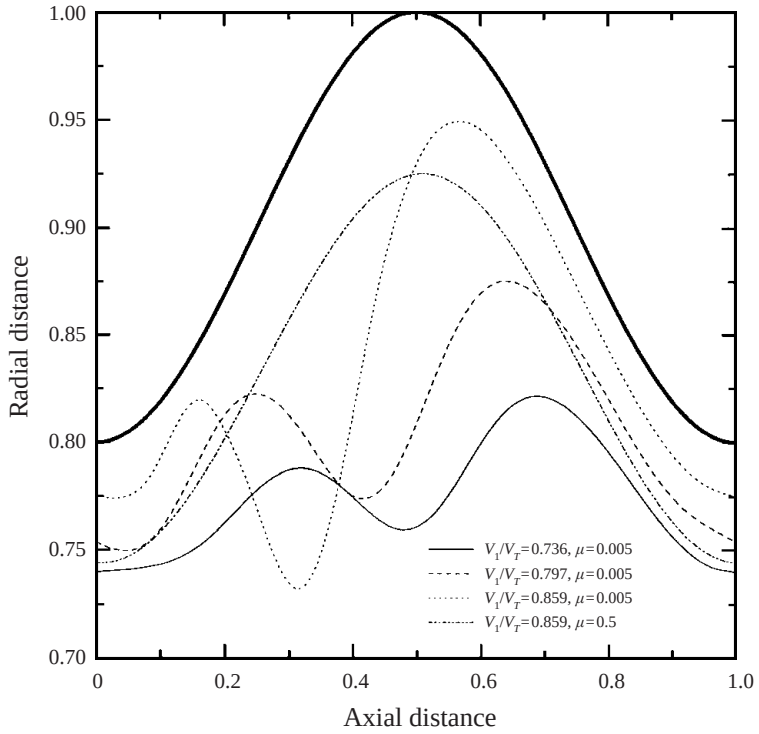

FIGURE 5. Effect of the ratio of volume occupied by the core fluid to the total volume of the tube and the viscosity ratio on the steady fluid/fluid interface, $\rho = 1$, $Re = 5$, $W = 10$, $\alpha = 0.8$, $\Lambda = 0.25\pi$, $N = 1$. The thickest line indicates the location of the tube wall.

occur at $Re = 1$, given the values of the rest of the parameters, but it does occur at $Re = 5$. This is shown in figure 6(b), where a large vortex appears inside the expanding portion of the tube and it is located entirely in the region occupied by the annular fluid. This vortex is not symmetric around the mid-plane and it arises first before the mid-plane as in this region the flow cross-section expands making the flow susceptible to separation. On increasing Re further, the vortex expands and moves toward the mid-plane. The onset of separation is dependent not only on the inertial forces, but also on the geometry (curvature) of the tube. The straight tube, for example, does not exhibit stationary flow separation irrespective of the value of Re. Decreasing the volume occupied by the inner fluid to $V_1/V_T = 0.736$ enlarges the recirculation region and the core fluid seems to bypass entirely the indentation of the tube, figure 6(c). Finally, increasing W to 20 does induce recirculation at parameter values for which it did not exist with $W = 10$, figure 6(d). This effect is accentuated further when $W = 40$.

9. Axisymmetric stability and energy analysis results

The neutral stability curves in this section are constructed by keeping constant all dimensionless numbers except one, while this remaining one, usually Re or μ, is varied until the system turns from stable to unstable or vice versa, i.e. the real part of the most 'dangerous' eigenvalue passes through zero. In the majority of the cases examined the most unstable eigenvalue is a complex one pointing to a Hopf bifurcation from the steady solutions, with the only exception when the viscosity ratio

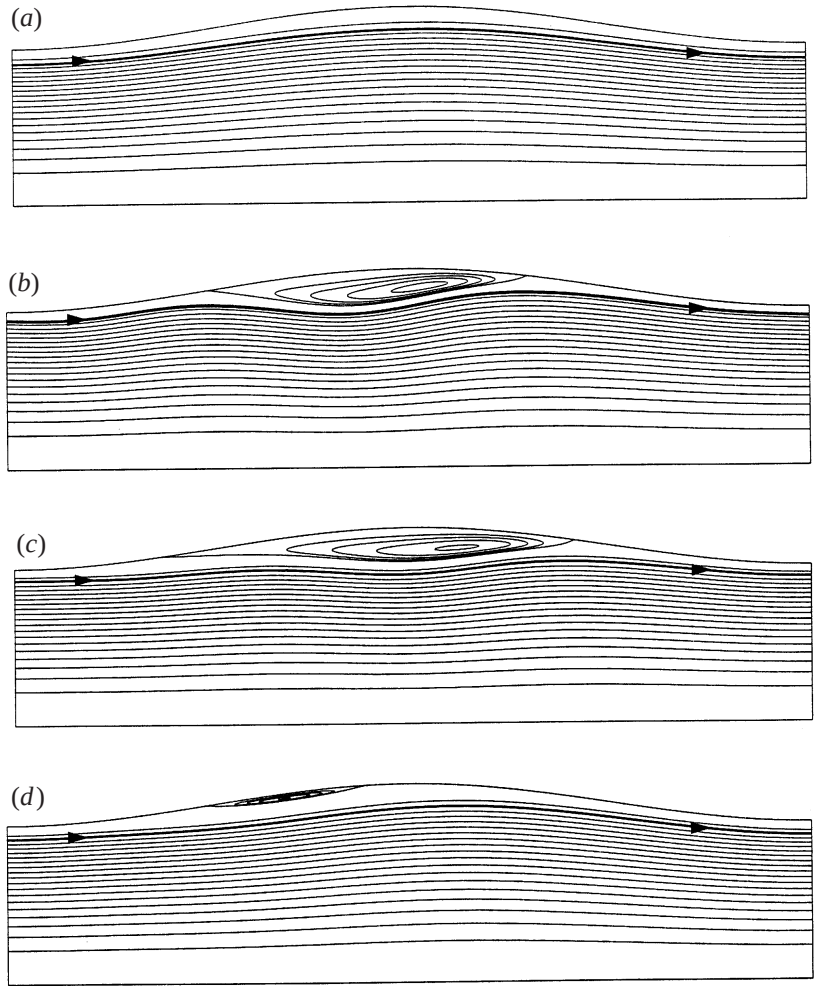

FIGURE 6. Streamlines corresponding to the steady flow with $\mu = 0.005$, $\rho = 1$, $\alpha = 0.8$, $\Lambda = 0.25\pi$, $N = 1$ and (*a*) $(Re, W, V_1/V_T) = (0.2, 10, 0.797)$; (*b*) $(5, 10, 0.797)$; (*c*) $(5, 10, 0.736)$; and (*d*) $(1, 20, 0.797)$.

becomes $O(10^{-3})$ and then the eigenvalues remain real. The change in the stability of the system is identified through extensive and very time-consuming eigenvalue calculations. The critical points are computed with a tolerance criterion as small as 0.5×10^{-3} for the most unstable eigenvalue. The use of the Arnoldi algorithm to expedite these computations is indeed essential.

The computation of only the critical value of the varying parameter is not adequate to determine the dominant mechanism that drives the instability and, for that reason, the latter is achieved in conjunction with the energy results reported in table 7. This is necessary, as there are many causes of instability such as viscosity stratification, capillarity and Reynolds stress, while in some cases the dominant mechanism may be a combination of the above. In straight tubes an estimation of the type of instability in CAF, whether it is an interfacial or a shear one, can be inferred by comparing the wavelength of the unstable mode with the radius of the core fluid. The instability driven by surface tension is characterized by long unstable waves, while the shear-

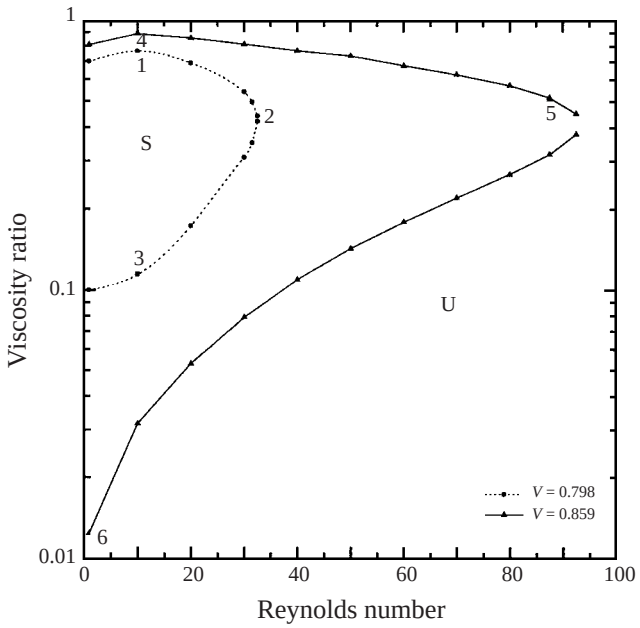

FIGURE 7. Effect of the volume ratio on the marginal stability curves as a function of the viscosity ratio and Reynolds number, $\rho = 1$, $W = 5$, $\alpha = 0.8$, $\Lambda = 0.25\pi$, $N = 5$. The numbers on the neutral curves indicate the points at which contributions to the linear energy have been calculated.

mode instability is connected with large Reynolds number in the less viscous fluid and unstable modes with short wavelength, Hu & Joseph (1989). In contrast, the existence here of a specific period of the geometry may alter this general picture. So we have to rely on the energy analysis, which identifies the source of instability by examining the relative magnitude of terms related to stresses acting tangent and normal to the interface and terms related to fluid inertia in its bulk.

First, neutral stability curves for constant W are presented in $\log(\mu)$ versus Re plots. In all cases these curves have an acute-angled shape within which the flow is stable. Their vertex is at higher Re and in the upper part μ varies a little between values close to, but smaller than, 1 and in the lower part both μ and Re vary considerably. It is noteworthy that, although there is an upper limit to the Reynolds number above which CAF turns from stable to unstable, no lower limit to Re exists for a wide range of viscosity ratios. In other words, as static conditions are approached, the expected capillary instability does not seem to arise, irrespective of the disturbance wavelength. This is explained by considering the fact that the growth rates for capillary instability are scaled with $T/(R\mu)$ (Chandrasekhar 1981, p. 540) which is proportional to Re^2W and which approaches zero much faster than Re does, when $W =$ constant. Therefore as $Re \to 0$, the growth rates also approach zero without changing sign, i.e. the flow remains stable.

Figure 7 shows the stability boundaries of CAF for the following values of the dimensionless numbers: $\rho = 1$, $W = 5$, $\alpha = 0.8$, $\Lambda = 0.25\pi$, $N = 5$ and shows the effect of the ratio of the volume of the core fluid to the total volume of the tube. These dimensionless numbers correspond to a sequence of five constrictions whose maximum radius is 0.125 times the length of each and its minimum radius is 0.8 times its maximum one. It is clear that by increasing the volume occupied by the core fluid the stable region expands and, as a result, the flow becomes unstable at much larger

Case	μ	ρ	Re	W	N	V_1/V_T	$RS_1 + RS_2$	B_N	B_T	$E \times 10^5$
1	0.7653	1	10	5	5	0.798	0.003	0.0143	**0.9826**	−0.343
2	0.41	1	32.5	5	5	0.798	0.0713	0.0951	**0.8335**	−0.2113
3	0.114	1	10	5	5	0.798	0.0695	0.0172	**0.9133**	−0.9468
4	0.8887	1	10	5	5	0.859	−0.0183	0.0671	**0.9512**	0.0225
5	0.5165	1	87.5	5	5	0.859	0.0832	0.0356	**0.8811**	−0.1884
6	0.0125	1	1	5	5	0.859	0.0115	0.0027	**0.9857**	−0.5011
7	0.8	1	1	10	5	0.859	−0.0004	0.0121	**0.9883**	0.0087
8	0.35	1	53	10	5	0.859	0.0759	0.0643	**0.8598**	−1.1
9	0.055	1	1	10	5	0.859	0.0008	0.0001	**0.9986**	−0.041
10	0.7	3	1	5	5	0.795	0.0003	0.0055	**0.9942**	−0.0765
11	0.5217	3	120	5	5	0.798	**0.4863**	**0.1772**	**0.3365**	9.15
12	0.01	3	3.782	5	5	0.798	**0.3619**	**0.6489**	−0.0118	−102.5
13	0.609	0.33	20	5	5	0.798	0.015	0.0126	**0.9724**	−0.054
14	0.17	0.33	1	5	5	0.798	0.0002	0.0005	**0.9993**	−0.0026
15	0.999	1	18	0.1543	2	0.859	−0.0029	**0.9887**	0.0143	0.5566
16	0.975	1	139.26	0.0026	2	0.859	0.0373	−0.313	**1.2757**	−0.0213
17	0.5	1	1.397	25.62	2	0.859	−0.0004	0.0016	**0.9988**	0.0115
18	0.07	1	1.881	14.1316	2	0.859	0.0021	0.0113	**0.9968**	0.1331
19	0.01	1	3.397	4.3329	2	0.859	**0.2128**	0.0407	**0.7464**	−0.8295
20	0.02	1	10.195	0.481	2	0.859	**0.3343**	0.0273	**0.6384**	0.0799

TABLE 7. Energy analysis results. Numbers in bold indicate the dominant term(s) in the energy balance.

values of the Reynolds number. Indeed, just a small increase in the volume ratio from 0.798 to 0.859 causes a significant increase in the maximum allowed Re, from about 32 to 95, while the value of the viscosity ratio which maximizes this critical value of Re remains approximately the same, $\mu \sim 0.45$. On the other hand, decreasing the volume ratio shrinks the stable domain and eventually leads to its disappearance. Similarly, Hu & Joseph (1989) have found that decreasing the thickness of the lubricating fluid in the annulus stabilizes CAF in a straight tube. It can also be seen that the steady flow remains stable within a range of values of μ. The viscosity ratio along the upper side of each angle is always below unity and its maximum values increase slightly (from 0.7 to 0.8) with increasing V_1/V_T, which means that the computed steady flow is physically realizable only when the more viscous fluid is centrally located. On the other hand, the viscosity ratio along the lower side of each angle decreases by about an order of magnitude and from 0.1 to 0.02 at small values of the Reynolds number by only changing V_1/V_T from 0.798 to 0.859.

Cases 1–3 in table 7 correspond to points on the dotted line in figure 7 with core volume ratio 0.798, while cases 4–6 correspond to points on the solid line with core volume ratio 0.859. These are three representative cases from each curve, having been chosen from their top, right and bottom segment, respectively, see figure 7. In spite of this, the various energy terms reveal that the dominant mechanism of instability is always due to the stresses that act in the direction tangent to the interface, since all the other energy terms are at least one order of magnitude smaller. Therefore, in all these cases instability is driven by viscosity stratification. The reason for this is that, although the basic state satisfies the interfacial balance on the undisturbed surface, it does not on the disturbed interface because of the jump in the shear stress there. Of course, this may not remain the dominant mechanism if one moves well into the unstable domain as Hu & Joseph (1989) did. It is worth noting that in none of the

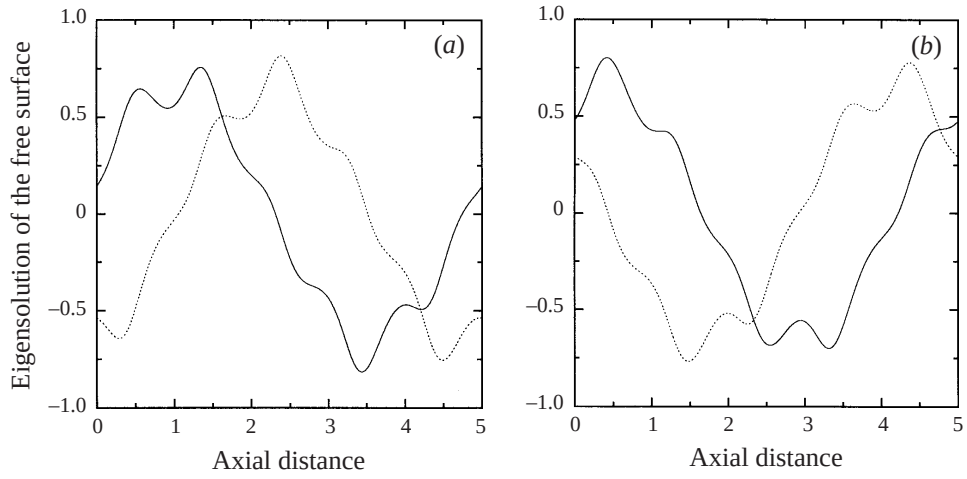

FIGURE 8. The shape of the disturbed interface corresponding to the critical point shown in table 7 as case 4, (*a*), and case 6, (*b*).

cases examined was a stable CAF with $\mu \geqslant 1$ found, irrespective of the values of the other dimensionless numbers, a result which is in agreement for the case of CAF in a straight tube reported by Preziosi *et al.* (1989).

Representative eigenforms of the fluid/fluid interface as well as of the streamfunction are given next. The two different curves in each of figures 8(*a*) and 8(*b*) correspond to the real (solid line) and imaginary (dotted line) parts of the eigenfunction of the interface, for cases 4 and 6 of figure 7, respectively. Rather small *Re*, but quite different values of μ (< 1) characterize these cases. It is observed that only one wavelength of the disturbance fits within the length of the tube, which in this case is 40 times its maximum radius. Clearly, these shapes resemble each other, but they deviate considerably from the eigenfunctions arising in a straight tube, which are simple sinusoidal waves of various wavelengths. In fact, on top of this single and dominant wave one may observe shorter ones with smaller amplitude. Figure 9(*a*) gives the part of the eigenfunction that corresponds to the fluid/fluid interface for case (*a*) in figure 7, where $Re = 80$, $\mu = 0.5717$, $\rho = 1$, $W = 5$, $\alpha = 0.8$, $\Lambda = 0.25\pi$, $N = 5$, $V_1/V_T = 0.859$. At this point the corresponding less stable eigenvalue is $-0.3174 \times 10^{-5} \pm 0.2381 \cdot \mathrm{i}$. Large *Re* and intermediate values of μ characterize this case. Here 2.5 wavelengths of the disturbance fit within the length of the tube and additional shorter waves arise on top of it too. Therefore, although *Re* is now larger than in figure 8, the most unstable disturbance is still characterized by a fairly long wavelength. Figures 9(*b*) and 9(*c*) give the part of the eigensolution corresponding to the instantaneous streamlines and verify its smoothness. The disturbance streamlines seem to form one large recirculating region, which includes two smaller ones in each undulation of the tube.

Figure 10 shows the effect of the inverse Weber number on the stability of the associated steady solution. The dimensionless numbers used are the following: $\rho = 1$, $V_1/V_T = 0.859$, $\alpha = 0.8$, $\Lambda = 0.25\pi$, $N = 5$. The two curves correspond to $W = 5$ and 10, respectively. It can be seen clearly that on increasing the capillary force on the fluid/fluid interface relative to fluid inertia in the core, the stable region of CAF is shrinking. Contributions to the disturbance energy are calculated for three representative points here as well. The results, given in table 7 (cases 7–9), reveal that the dominant mechanism of instability is due to tangential stresses on the interface (as

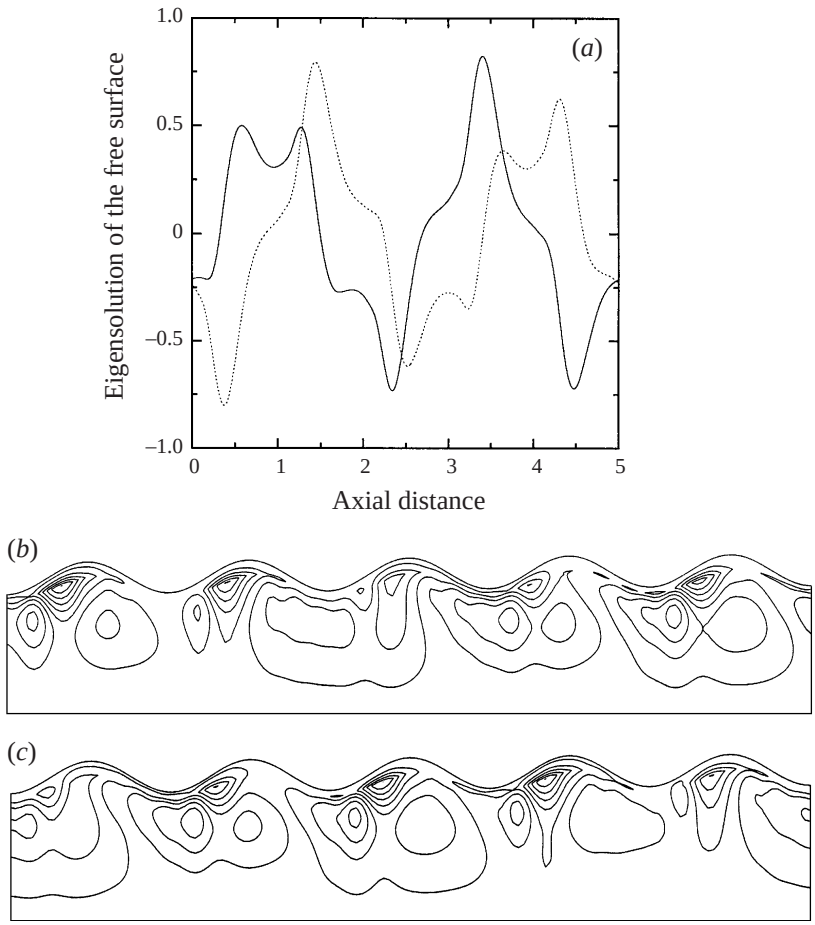

FIGURE 9. (*a*) Disturbed shape of the interface for the case for large Re and W shown in table 7 as case 5. The corresponding critical point is indicated in figure 7 by (*a*). Parameter values are: $\mu = 0.5717$, $\rho = 1$, $Re = 80$, $W = 5$, $V_1/V_T = 0.859$, $\alpha = 0.8$, $\Lambda = 0.25\pi$, $N = 5$, and the corresponding eigenvalue $\sigma = -0.3174 \times 10^{-5} \pm 0.2381 \cdot \mathrm{i}$. (*b*),(*c*) Real and imaginary parts, respectively, of the associated disturbed streamlines.

in cases 1–6) caused by the viscosity difference between the two fluids. Additionally, the eigenshapes are again characterized by long waves. Because surface tension generally contributes to the destabilization of long waves, it is understandable that increasing W promotes the instability. This effect of W on the neutral stability curves is not different from that caused by the variation of V_1/V_T, because increasing V_1/V_T or effectively the average R_1, and decreasing W or effectively the surface tension, decreases the capillary force on the interface. Nevertheless, one may still wonder why changing W relocates the neutral curves, although energy analysis indicates that instability is induced by viscosity difference. We believe that this is because on increasing W the interface in the base state becomes more deformed, and susceptible to shear instability. This effect is not present in CAF in a straight tube, where the base state is straight also and remains unaffected by variations in W or Re.

As mentioned already, in the present case normal mode decomposition in the axial direction is not possible, because the periodic constrictions force the primary flow to depend on the axial direction. Although this does not seem to impose a major

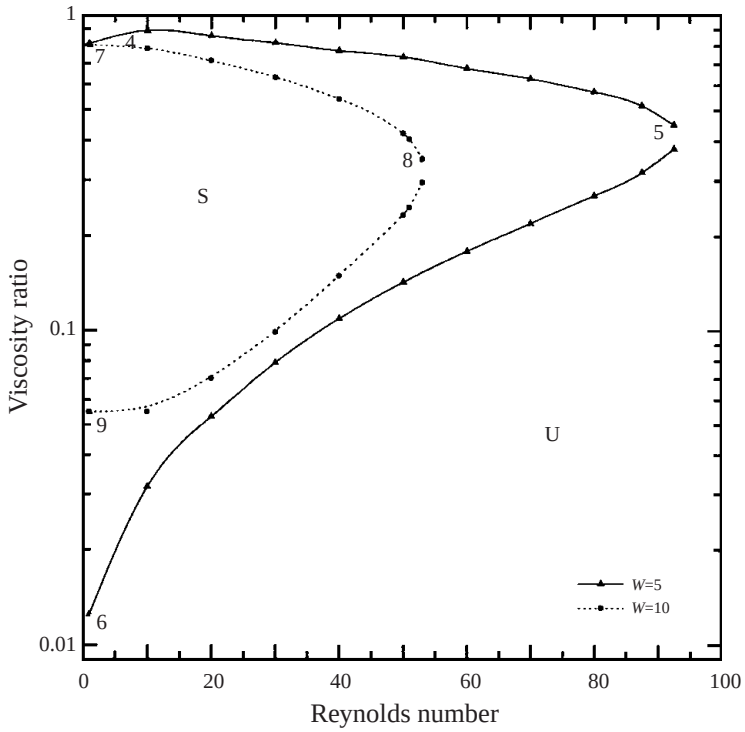

FIGURE 10. Effect of the inverse Weber number on the marginal stability curves as a function of the viscosity ratio and Reynolds number, $\rho = 1$, $\alpha = 0.8$, $V_1/V_T = 0.859$, $\Lambda = 0.25\pi$, $N = 5$. The numbers on the neutral curves indicate the points at which contributions to the linear energy have been calculated.

numerical problem, it does make the stability analysis rather more difficult and time-consuming, since all modes must be computed simultaneously and their dependence in the radial and axial direction cannot be separated. In contrast, in a straight tube one needs to solve only for the eigenvectors in the radial direction irrespective of the axial length considered. In all the simulations that we have performed we have tried to minimize as much as possible the effect of the finite axial length and the related periodic boundary conditions. For this reason we have used in most cases five undulations in the tube with aspect ratio $L/R_{max} = 8$ which results in a total computational length 40 times the maximum radius of the tube. In order to verify that this is indeed necessary, the effect of the number of undulations considered on the stability of CAF is examined for $N = 1, 2$ and 5. In all three cases it is verified first that the independently calculated base solution is periodic with period L, not NL. However, figure 11 shows that N has a profound effect on the stability limits of the flow. The instability predicted by the curves in this figure is again due to the viscosity contrast of the two fluids. As in figures 7 and 10, it is a long-wave instability and, although the stable region of CAF shrinks considerably on increasing N from 1 to 5, the dominant mechanism of instability does not change at all. Comparing the curves in figure 11 it is concluded that using just one undulation gives erroneous results for flow stability, whereas using five is more than adequate, since results for two and five undulations are very close to each other. Close observation of figure 11 reveals that stability is predicted even wmth $\mu = 1.008 > 1$, when $N = 1$, which is clearly wrong. Similarly, we have found that stable flow for even larger values of μ

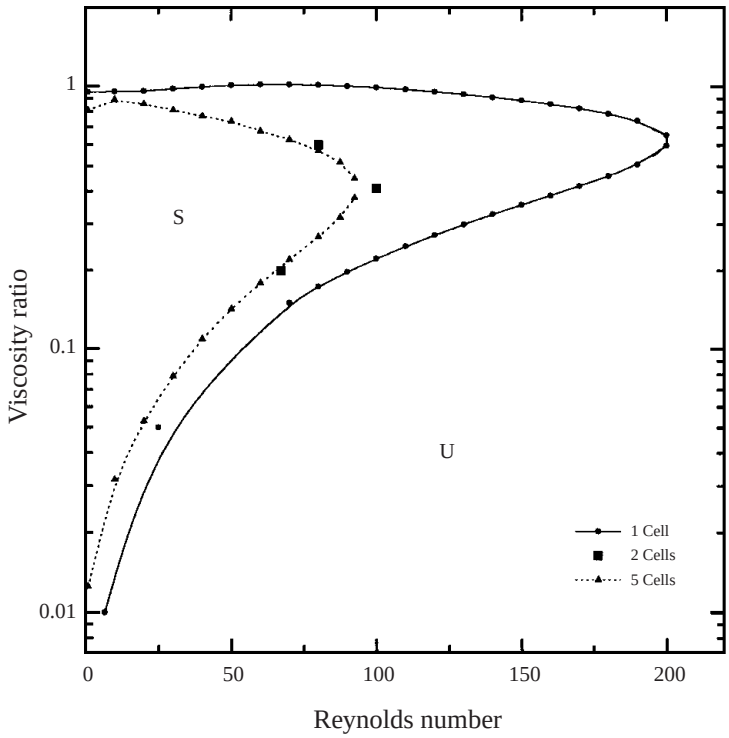

FIGURE 11. Effect of the number of undulations on the marginal stability curves as a function of the viscosity ratio and Reynolds number, $\rho = 1$, $W = 5$, $\alpha = 0.8$, $V_1/V_T = 0.859$, $\Lambda = 0.25\pi$.

(e.g. $\mu = 5$) may be predicted, if the aspect ratio, Λ, is not taken to be small enough with $N = 1$. It seems that keeping only one undulation does not provide enough space for the instability to develop. Therefore, the effect on stability of imposing periodic boundary conditions in a finite domain is reduced considerably when using at least $N = 2$. Although in figure 11 we increase the number of cells above two and, therefore, we permit modes with greater wavelength, these are stable. Clearly, the stable domain does not vanish as N increases. It is worth noting that five undulations is the maximum number that we can handle as dictated by the computer memory and CPU time requirements. Of course this result does not mean that the critical modes computed using $N = 2$ and $N = 5$ are the same and for that reason the corresponding critical values of μ and Re are slightly different. What is happening is that although the critical mode changes with increasing the length of the domain, the difference of the critical value of the parameter at which the bifurcation takes place changes less and less, indicative of its convergence with respect to the length of the domain.

In general, on comparing stability results for straight and undulating tubes it is found that the latter imposes stricter limits on the parameter values and therefore as the constriction ratio approaches unity the above stable domains expand. Preziosi *et al.* (1989), following the methodology introduced by Yih (1967), have examined the stability of CAF in a straight tube witih respect to long waves. They have found that the Reynolds number should be large enough in order to overcome the destabilizing effect of surface tension. More specifically, they have predicted that for a case with $\mu = 0.5$, $\rho = 1$, $V_1/V_T = 0.859$, upon transforming results from their figure 3 to our

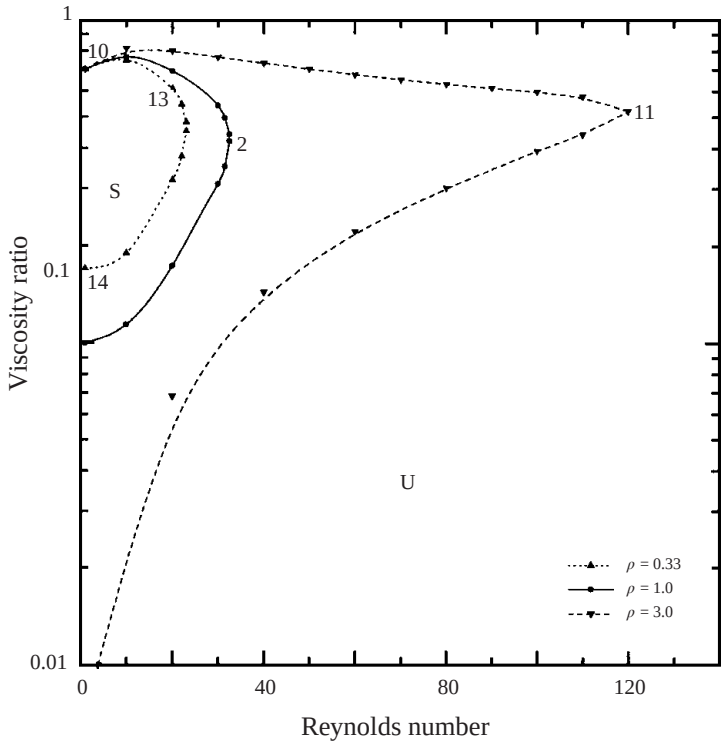

FIGURE 12. Effect of the density ratio on the marginal stability curves as a function of the viscosity ratio and Reynolds number, $W = 5$, $\alpha = 0.8$, $V_1/V_T = 0.797$, $\Lambda = 0.25\pi$, $N = 5$. The numbers on the neutral curves indicate the points at which contributions to the linear energy have been calculated.

variables, requires $W < 12$ to be stable, i.e. a larger upper limit than in a constricted tube.

In figure 12 we present the effect of the density ratio on the stability of CAF in an undulating tube. It is observed that for all values of the viscosity ratio the use of a lighter fluid in the core expands the stable region of CAF in a periodically constricted tube to larger values of the Reynolds number. Cases 13 and 14 of table 7 reveal that, when the annular fluid is the lighter one, instability is generated by the tangential stresses on the interface, while cases 10–12 show that, when the annular fluid is the heavier one, this mechanism holds only for viscosity ratio above 0.7. In contrast, when the viscosity ratio is below 0.5 a change in the mechanism of instability occurs and it is now driven by either capillarity or by the Reynolds stress or a combination of both. This change in the mechanism of instability is why the third curve, with $\rho = 3$, deviates so much from the other two, which have density ratio $\rho = 0.33$ and 1. For example, the maximum Re is restricted to values below 20 for $\rho = 0.33$, below 30 for $\rho = 1$ and is somewhat above 120 for $\rho = 3$. Therefore, when surface tension is comparable to inertial forces, $W \sim 5$, the use of a lighter fluid in the core can suppress the more unstable long waves which are excited by the stresses tangent to the interface for $\rho = 1$, whereas now all possible mechanisms combine to generate instability. This stabilization is greater for intermediate values of the viscosity ratio, $\mu \sim 0.5$. Smith (1989) examined the effect of the density difference on the long-wave instability of CAF in a straight tube. He considered fluids of equal viscosities, so as

to suppress Yih's type of instability, and allowed fluids of different densities. He took into account the effect of gravity in order to produce a jump in the curvature of the steady velocity profile and showed that, indeed, the density contrast of the two fluids can suppress or excite unstable modes of long wavelength. In our case, the jump in the shear stress is not caused by gravity and density difference, but by the viscosity difference of the two fluids. The density difference affects the stability of CAF in a constricted tube in the same way as in a straight tube, as it multiplies the inertial terms of the outer fluid, in this way modifying its pressure. The pressure of the outer fluid is involved in the normal force balance and, for this reason, the increase of the density ratio brings into play the energy term related to the interfacial forces acting in the direction normal to the interface and the term related to the fluid inertia, see table 7.

We define the parameter

$$J = \frac{T R_{max}\,\hat{\rho}_1}{\hat{\mu}_1^2}\Lambda^2 = W\,Re^2,$$

which is the inverse Ohnesorge number. The advantage of using this parameter for setting the interfacial tension is that it is independent of the velocity of the basic flow and it is determined only by the tube geometry and the properties of the two fluids; thus it characterizes the fluids. So, we have constructed the figures that follow using J instead of W. In these we re-examine the effect of the volume ratio, the density ratio and the effect of J itself on the stability of CAF in an undulating tube and observe a common characteristic that distinguishes them from all the earlier stability diagrams. Plainly, in all of them we identify neutral stability boundaries at small as well as large Reynolds numbers. The stable domains now resemble a triangle in $\log(\mu)$ versus $\log(Re)$ plots, with a top side (where the viscosity ratio tends to unity), a lower left, almost vertical side (where Re remains small) and a lower right side. Along each neutral curve with a constant value of J the fluid pair remains the same and increasing Re by one or two orders of magnitude requires a decrease in W by two or four orders of magnitude, respectively, whereas moving along the previous neutral curves with constant W requires changing the fluid pair appropriately.

Moreover, figure 13 shows that by increasing the volume of the high-viscosity, inner fluid the stable region of CAF generally expands. This expansion is quite clear in the lower two sides of the neutral curve including both low and high Reynolds numbers, but not in most of its upper side. This is not the case in the upper part of the neutral curves when W is kept constant (figure 7), which is significantly affected and has been associated with instability due to viscosity stratification. Therefore, the instability generating most of the upper part of the curves in figure 13 should not be associated with the viscosity difference. Besides, in this segment, $1-\mu$ is so close to zero that it would eliminate the related energy term. Regarding the remaining instability mechanisms – the action of the normal stresses or the inertia of both fluids – the second is associated with the outer fluid, which is the less viscous one, see Hu & Joseph (1989). However, if this is the instability mechanism, then the increase of the volume of the inner fluid should modify them significantly, because increasing the volume of the inner fluid decreases the mass of the outer one and, thus, its ability to destabilize the flow through the Reynolds stresses. Since this is not observed, this mechanism should be excluded also and the instability should be attributed to capillarity. Indeed this conclusion is in accordance with the energy calculations reported in table 7 (case 15). On examining the energy terms in the remaining segments of the neutral curves in figure 13, it is found that the dominant mode of instability at the limit of small viscosity ratio, cases 19 and 20, is a combination of the action of the Reynolds stress

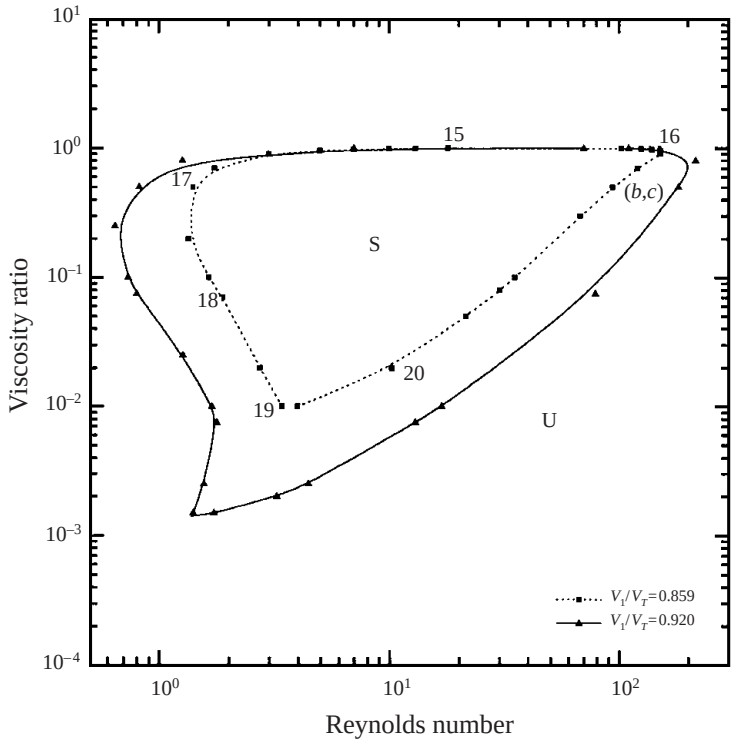

FIGURE 13. Effect of the volume ratio occupied by the core fluid on the marginal stability curves as a function of the viscosity ratio and Reynolds number keeping constant the Ohnesorge number, $\rho = 1$, $J = 50$, $\alpha = 0.8$, $\Lambda = 0.25\pi$, $N = 2$. The numbers on the neutral curves indicate the points at which contributions to the linear energy have been calculated.

and the stresses acting tangent to the interface. This result should be expected, as when the viscosity of the outer fluid becomes so much smaller than that of the inner fluid, the effective *Re* of the outer fluid increases. Finally, the neutral stability curves at lower and higher Reynolds numbers and intermediate values of viscosity ratio are associated with viscosity stratification (see table 7, cases 16–18). Still, one may wonder why at least in the left lower segment where *Re* is small (which necessitates large *W* values for a constant and large *J*) we do not observe capillary instability. Again we believe that capillarity is involved, but in a more subtle way: the 'large' *W* values do perturb the base interface shape, but do not cause the instability which is driven by the higher shear exerted on the more wavy interface.

Representative eigenforms of the fluid/fluid interface for the above cases 17, 19 and 20 are given in figure 14. (The solid and the dotted line in each figure correspond to the real and the imaginary part, respectively.) The first two cases cover the lower left segment of the neutral stability boundary and have quite different values of μ and *Re*. They exhibit a single wavelength in an axial distance that is 16 times longer than the maximum radius of the tube. The decrease in μ while moving from case 17 to case 19 decreases the smoothness of the interface and gives rise to additional shorter and smaller waves. The disturbance interfaces for cases 15 and 18 closely follow those of case 17. On the other hand, case 20 belongs to the lower right segment with a very small value of μ, but an intermediate value of *Re*. Now the interface is even less smooth and two wavelengths appear in the same axial distance. Similarly, case 16 with

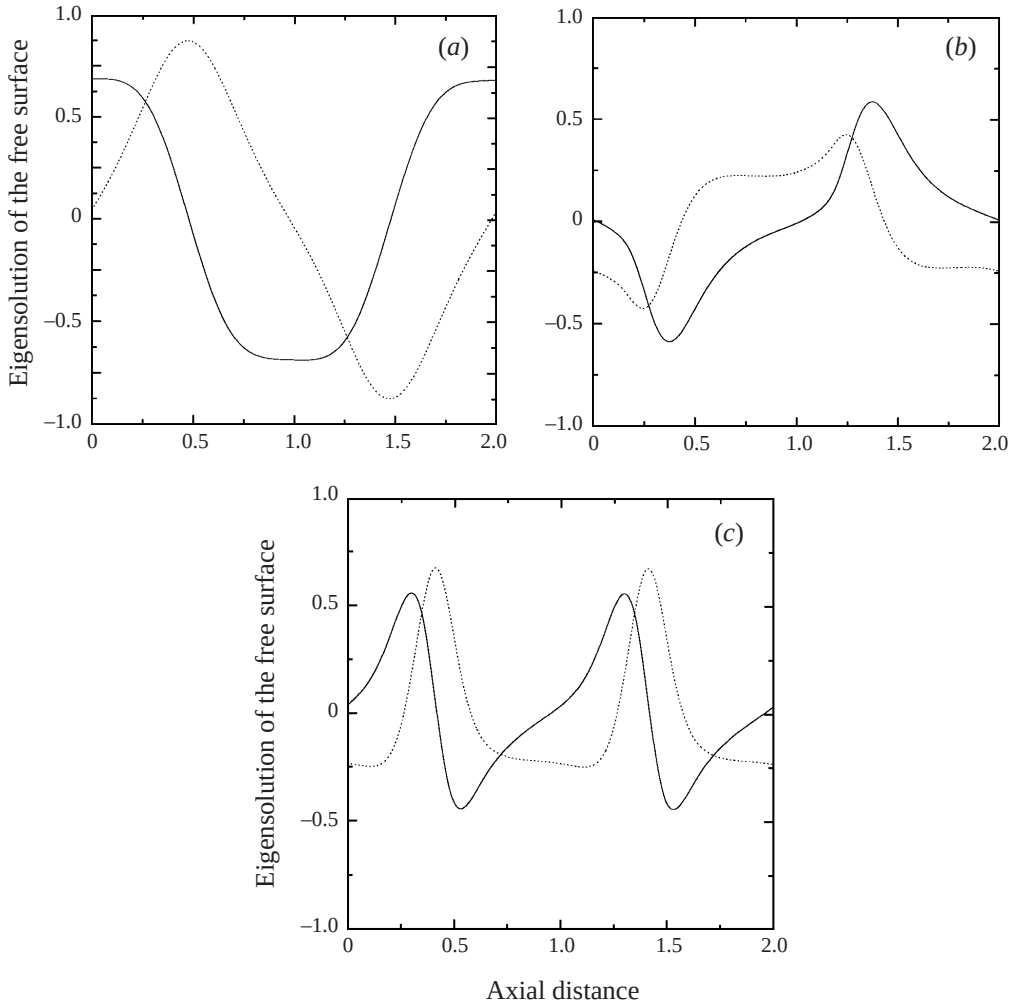

FIGURE 14. The shape of the distrubed interface corresponding to the critical points shown in table 7 as case 17, (*a*), case 19, (*b*), and case 20, (*c*).

quite large *Re*, but μ very close to unity has three wavelengths. Thus, all these cases could be characterized as disturbances with intermediate wavelengths, which are not simple sinusoidal waves. Figures 15 and 16 correspond to cases 'b' and 'c' in figure 13 with the following values of the dimensionless numbers: $Re = 93.89$, $\mu = 0.5$, $\rho = 1$, $W = 0.5672 \times 10^{-2}$, $\alpha = 0.8$, $\Lambda = 0.25\pi$, $N = 2$, $V_1/V_T = 0.859$ and with the following eigenvalues: $-0.4750 \times 10^{-4} \pm 0.1926 \times 10^{1}$, $0.3729 \times 10^{-4} \pm 0.2256 \times 10^{1}$, respectively. In these neighbouring cases at large *Re*, but very small *W*, the disturbance interfaces have either six or seven wavelengths in the same axial distance, i.e. they are somewhat shorter than all previous cases. Clearly when surface tension is significant relative to inertia then, irrespective of *Re*, the shape of the interface is quite smooth and rapid changes are suppressed. The opposite holds when surface tension is very small relative to inertia, where short-wavelength, unstable modes appear. Figures 15(*b*) and 16(*b*) give the part of the eigensolution corresponding to the streamlines and verify its smoothness. The disturbance streamlines now seem to form two larger recirculating

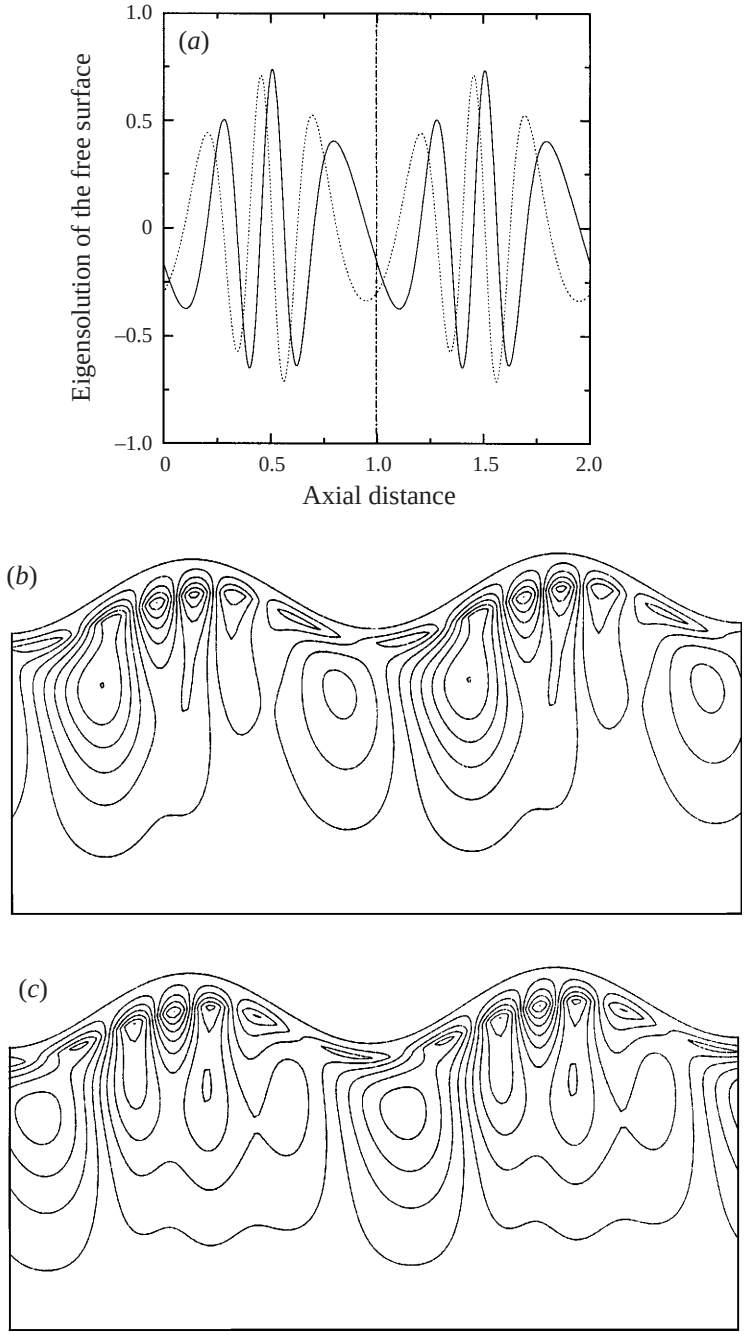

FIGURE 15. (*a*) Computed disturbed shape of the interface for the case of large Reynolds number and small surface tension. The corresponding critical point is indicated in figure 13 by (*b*). The parameter values are: $\mu = 0.5$, $\rho = 1$, $Re = 93.89$, $W = 0.005672$, $V_1/V_T = 0.859$, $\alpha = 0.8$, $\Lambda = 0.25\pi$, $N = 2$, and the eigenvalue is $\sigma = -0.4750 \times 10^{-4} \pm 0.1926 \times 10^{1}\cdot$i. (*b*),(*c*) Real and imaginary parts, respectively, of the associated disturbed streamlines.

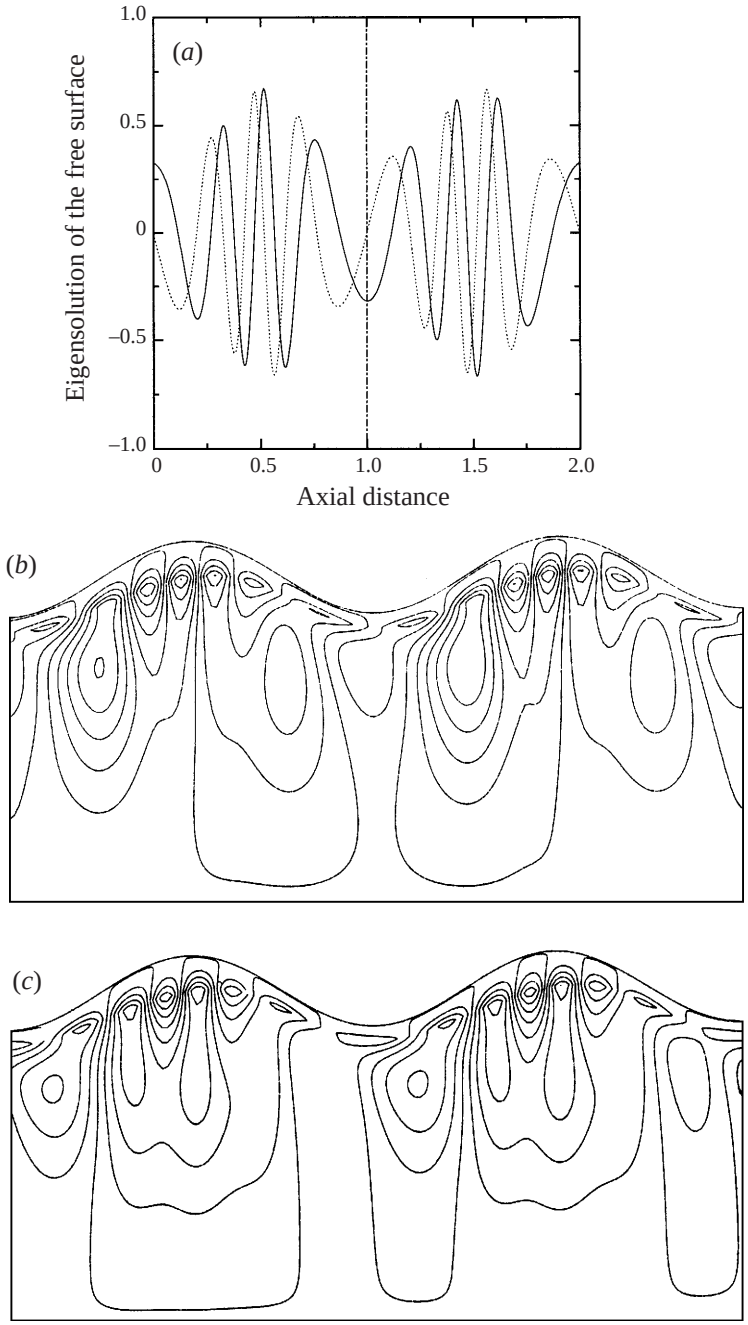

FIGURE 16. (*a*) Computed disturbed shape of the interface for the same values of the dimensionless numbers as in figure 15, but with computed eigenvalue $\sigma = 0.3729 \times 10^{-4} \pm 0.2256 \times 10^{1} \cdot \mathrm{i}$. The corresponding critical point is indicated in figure 13 by (*c*). (*b*),(*c*) Real and imaginary parts, respectively, of the associated disturbed streamlines.

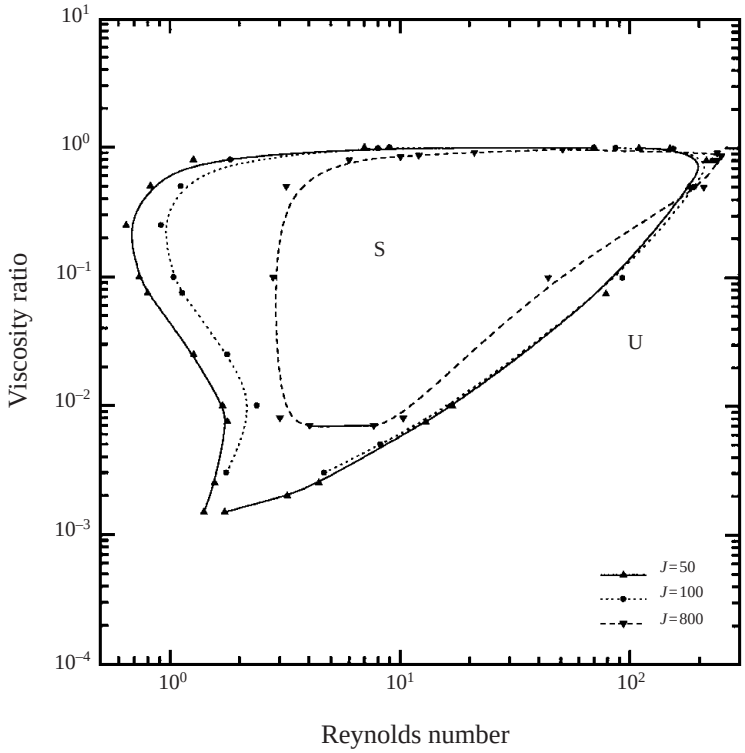

FIGURE 17. Effect of the inverse Ohnesorge number on the marginal stability curves as a function of the viscosity ratio and Reynolds number, $\rho = 1$, $V_1/V_T = 0.920$, $\alpha = 0.8$, $\Lambda = 0.25\pi$, $N = 2$.

regions side by side, which contain three or more smaller ones in each undulation of the tube.

In figure 17 we examine the effect of the inverse Ohnesorge number. In general, increasing J decreases the stable domain, but less severely than increasing W (compare with figure 10). The lower-left branch of the neutral stability curves, on which instability is generated by the viscosity difference, seems to be affected most by this increase. This is explained by noticing that increasing J at these small and constant Re values increases W proportionately, and keeps it large, which deforms the base state, making it more susceptible to shear instability. Similar qualitatively, but smaller quantitatively, is the effect of increasing J on the lower-right side of the stability boundary, because now Re is larger and W assumes quite smaller values. At the largest Re where W is very small, and in a small range of intermediate μ values, the effect of J is reversed; increasing it expands the stable domain. Finally, increasing J from 50 to 100 leaves unaffected most of the upper boundary and it takes a further increase in J by a factor of 8 to reduce by just half its portion that remains unaffected. This could be puzzling because it has been shown that instability in this part of the boundary is due to capillarity. Its explanation relies on the fact that when, for example, $Re = 20$, increasing J from 100 to 800, increases W from 0.25 to only 2.0, i.e. the inverse Weber number varies between smaller values.

In figure 18 we present the effect of the density ratio. In general increasing ρ expands the stable domain and each successive domain seems to fully enclose the previous one. Now both the left and right lower boundaries expand at about the same

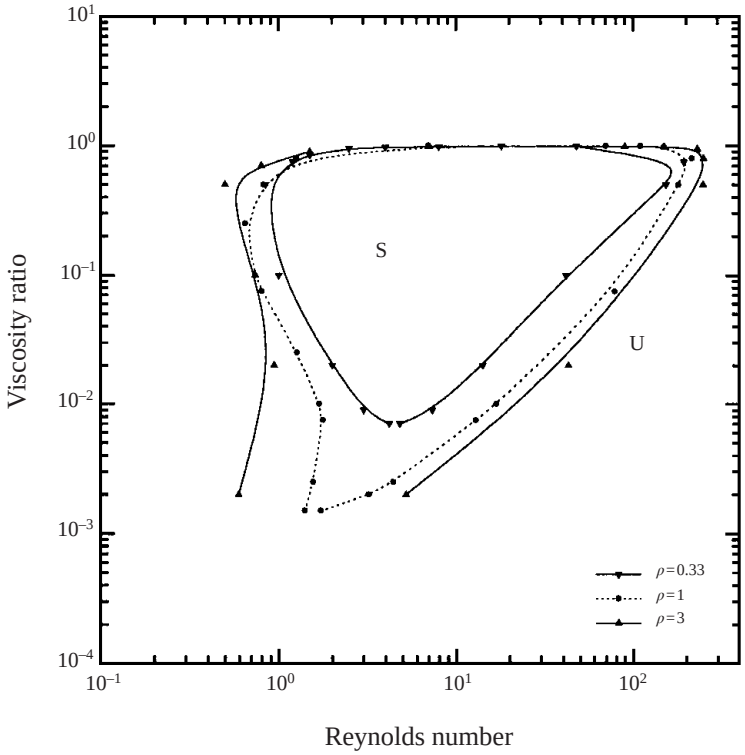

FIGURE 18. Effect of the density ratio on the marginal stability curves as a function of the viscosity ratio and Reynolds number keeping constant the Ohnesorge number, $V_1/V_T = 0.920$, $J = 50$, $\alpha = 0.8$, $\Lambda = 0.25\pi$, $N = 2$.

rate. At the largest ρ value that we examined, convergence of the base solution at very small values of $\mu \sim 10^{-3}$ was not achieved. This implies that a steady state may not exist. It is only here as well as in figures 13 and 17, that the critical eigenvalues at the very small values of μ ($\mu \sim 2 \times 10^{-3}$) are real and not complex. Calculations using our spectral code for these very small values of the viscosity ratio, which promotes the formation of a strong vortex in the annular fluid, are still accurate, but considerably more difficult to converge.

10. Closing remarks

Core–annular flow of two immiscible fluids in a periodically constricted tube has been studied. The governing equations are written in the vorticity–streamfunction formulation for studying two-dimensional flow and its stability. Both the variable tube radius and, even more so, the unknown location of the fluid/fluid interface necessitate the use of a non-orthogonal coordinate transformation into a fixed and simple domain. Its boundaries are chosen so that they facilitate the use of a pseudo-spectral representation of all the dependent variables, which is preferred for its exponential convergence. Newton–Raphson iterations are employed for the calculation of steady solutions and the Arnoldi algorithm for the calculation of the most dangerous eigenvalues. The steady-state results and the eigenvalues have been checked for convergence by increasing the number of collocation points, and against results reported in the literature for limiting values of the parameters.

At low values of Re, the streamlines follow the tube boundary and exhibit the expected symmetry at creeping flow conditions. Increasing Re or W or decreasing the constriction or the viscosity ratio breaks this symmetry and eventually induces recirculation in the part of the tube with the increasing cross-section. Varying the volume of the inner fluid with respect to the volume of the tube also affects the size and the intensity of the recirculation.

Stability has been examined by generating neutral curves in μ versus Re plots. The mechanism creating it has been explored by calculating the various contribution to the energy budget. It has been found that when W is kept constant the neutral curves have an acute angled shape with their vertex in the large-Re area, an upper side almost parallel to and always below the $\mu = 1$ line and a lower side along which both μ and Re vary considerably. At these boundaries a Hopf bifurcation from the steady base state takes place. A stability boundary at low Re does not arise in this case, because the eigenvalues, without changing sign, approach zero from within the stable domain at the same rate that Re does. It has been shown that sufficient length of the tube must be used in the stability calculations, in order that they are unaffected by the boundary conditions imposed at both ends of the tube. It has been found that the stability boundaries expand on increasing V_1/V_T, decreasing W, and using a more dense fluid in the annulus, and an explanation provided. Furthermore, a value of the viscosity ratio exists, always below unity, that maximizes the range in Re for which the steady flow remains stable. In most cases, steady states that exhibit recirculation are unstable. In all cases with $\rho \leqslant 1$ the energy analysis showed that instability is generated by viscosity stratification and the wavelength of the most critical disturbance is of the order of the tube length, but it does not have a simple sinusoidal shape.

Similar stability calculations have been performed keeping J, which is independent of the adopted characteristic velocity, constant. The major differences in the new results from those in the previous case are that: (i) a stability boundary arises even at low Re and, thus, the stable domain resembles a triangle; (ii) the two lower sides of this triangle may intersect each other at very small values of μ making the convergence of the computations more difficult, and the related critical points have real eigenvalues; (iii) the wavelength of the neutral disturbances are shorter than those for constant W and in some cases they may be characterized as short; and (iv) instability is generated by capillarity or a combination of Reynolds stresses and capillarity when $\mu \to 1$, whereas these mechanisms seem to prevail for $\mu < 0.5$ and $\rho > 1$ when W is kept constant.

Although the present results predict oscillatory flow outside the domains defined by the neutral curves, certain assumptions need to be removed in order to be able to allow for large deformations of the interface (beyond the linear regime) and to predict its breakup and the formation of slugs (i.e. pulsing flow). Some of our results along these lines have already been reported elsewhere (Kouris & Tsamopoulos 1999), whereas a thorough study of the nonlinear dynamics of CAF in a straight tube will appear in Kouris & Tsamopoulos (2001*a*, *b*) and a comparative study of solution methods of CAF in a constricted tube including three-dimensional stability will appear in Kouris *et al.* (2000).

This work was partially supported under the EPET II program (Grant number 550) of the General Secretariat of Research and Technology of Greece and under the EPEAEK program (Grand number 51) of the Ministry of Education of Greece.

REFERENCES

Amon, C. H., Guzman, A. M. & Morel, B. 1996 Lagrangian chaos, Eulerian chaos, and mixing enhancement in converging-diverging channel flows. *Phys. Fluids* **8**, 1192–1206.

Anturkar, N. R., Papanastasiou, T. C. & Wilkes, J. O. 1991 Stability of coextrusion through converging dies. *J. Non-Newtonian Fluid Mech.* **41**, 1–26.

Aul, R. W. & Olbricht, W. L. 1990 Stability of a thin annular film in pressure-driven flow though a capillary. *J. Fluid Mech.* **215**, 585–599.

Boomkamp, P. A. M. & Miesen, R. H. M. 1997 Classification of instabilities in parallel two-phase flow. *Intl J. Multiphase Flow* **22**, 67–88.

Canuto, C., Hussaini, M. Y., Quarteroni, A. & Zang, T. A. 1988 *Spectral Methods in Fluid Dynamics*. Springer.

Chandrasekhar, S. 1981 *Hydrodynamic and Hydromagnetic Stability*. Dover.

Charles, M. E., Govier, G. W. & Hodgson, G. W. 1961 The horizontal pipeline flow of equal density of oil-water mixtures. *Can. J. Chem. Engng* **39**, 17–36.

Christodoulou, K. N. & Scriven, L. E. 1988 Finding leading modes of a viscous free surface flow: an asymmetric generalized eigenproblem. *J. Sci. Comput*. **3**, 355–406.

Deiber, J. A. & Schowalter, W. R. 1979 Flow through tubes with sinusoidal axial variations in diameter. *AIChE J.* **25**, 638–645.

Gottlieb, D. & Orszag, S. A. 1977 *Numerical Analysis of Spectral Methods: Theory and Applications*. SIAM.

Guzman, A. M. & Amon, C. H. 1996 Dynamical flow characterization of transitional and chaotic regimes in converging-diverging channels. *J. Fluid Mech.* **321**, 25–57.

Hickox, C. E. 1971 Instability due to viscosity and density stratification in axisymmetric pipe flow. *Phys. Fluids* **14**, 251–262.

Hooper, A. P. & Boyd, W. G. C. 1983 Shear-flow instability at the interface between two viscous fluids. *J. Fluid Mech.* **128**, 507–528.

Hu, H. H. & Joseph, D. D. 1989 Lubricated pipelining: stability of core-annular flow. Part 2. *J. Fluid Mech.* **205**, 359–396.

Hu, H. H. & Patankar, N. 1995 Non-axisymmetric instability of core-annular flow. *J. Fluid Mech.* **290**, 213–243.

Huang, A. & Joseph, D. D. 1995 Stability of eccentric core annular flow. *J. Fluid Mech.* **282**, 233–245.

Joseph, D. D. 1973 Domain perturbations: the higher order theory of infinitesimal water waves. *Arch. Rat. Mech. Anal.* **51**, 295–303.

Joseph, D. D., Bai, R., Chen, K. P. & Renardy, Y. Y. 1997 Core-annular flows. *Ann. Rev. Fluid Mech.* **29**, 65–90.

Joseph, D. D. & Renardy, Y. 1993 *Fundamentals of Two-Fluid Dynamics, Part II Lubricated Transport, Drops and Miscible Fluids*. Springer.

Joseph, D. D., Renardy, M. & Renardy, Y. 1984 Instability of the flow of two immiscible liquids with different viscosities in a pipe. *J. Fluid Mech.* **141**, 309–317.

Kerchman, V. 1995 Strongly nonlinear interfacial dynamics in core-annular flows. *J. Fluid Mech.* **290**, 131–166.

Kouris, Ch., Neophytides, St., Vayenas, C. G. & Tsamopoulos, J. 1998 Unsteady state operation of catalytic particles with constant and periodically changing degree of external wetting. *Chem. Engng Sci.* **53**, 3129–3142.

Kouris, Ch., Dimakopoulos, Y., Georgiou, G. & Tsamopoulos, J. 2000 Comparison of spectral and finite element methods applied to the study of interfacial instabilities of core-annular flow in an undulating tube. *Intl J. Numer. Meth. Fluids* (submitted).

Kouris, Ch. & Tsamopoulos, J. 1999 Linear and nonlinear analysis of interfacial instabilities in two-phase flow in straight and constricted tubes. In *Two-Phase Flow Modeling and Experimentation* (ed. G. Celata, P. DiMarco & R. Shah), pp. 1577–1584. Edizioni ETS, Pisa.

Kouris, Ch. & Tsamopoulos, J. 2000 Concentric core-annular flow in a circular tube of slowly varying cross-section. *Chem. Engng Sci.* **55**, 5509–5530.

Kouris, Ch. & Tsamopoulos, J. 2001*a* Dynamics of axisymmetric core-annular flow I. The more viscous fluid in the core, bamboo waves. *Phys. Fluids* (accepted).

Kouris, Ch. & Tsamopoulos, J. 2001*b* Dynamics of axisymmetric core-annular flow II. The less viscous fluid in the core, saw tooth waves. *Phys. Fluids* (submitted).

Lahbabi, A. & Chang, H.-C. 1986 Flow in periodically constricted tubes: transition to inertial and nonsteady flows. *Chem. Engng Sci.* **41**, 2487–2505.

Lehoucq, R. B. & Scott, J. A. 1996 An evaluation of software for computing eigenvalues of sparse nonsymmetric matrices. *MCS*-P547–1195. Argonne National Laboratory.

Melli, T. R., De Santos, J. M., Kolb, W. B. & Scriven, L. E. 1990 Concurrent downflow in networks of passages. Microscale roots of macroscale flow regimes. *Ind. Engng Chem. Res.* **29**, 2367–2379.

Oliemans, R. V. & Ooms, G. 1986 Core-annular flow of oil and water through a pipeline. In *Multiphase Science and Technology*, Vol. 2 (ed. Hewitt, Delhaye & Zuber). Hemisphere.

Papageorgiou, D. T., Maldarelli, C. & Rumschitzki, D. S. 1990 Nonlinear interfacial stability of core-annular film flows. *Phys. Fluids* **2**, 340–352.

Payatakes, A. C. 1982 Dynamics of oil ganglia during immiscible displacement in water-wet porous media. *Ann. Rev. Fluid Mech.* **14**, 365–393.

Pilitsis, S. & Beris, A. N. 1989 Calculations of steady-state viscoelastic flow in an undulating tube. *J. Non-Newtonian Fluid Mech.* **31**, 231–287.

Preziosi, L., Chen, K. & Joseph, D. D. 1989 Lubricated pipelining: stability of core-annular flow. *J. Fluid Mech.* **201**, 323–356.

Rayleigh, Lord 1879 On the stability of jets. *Proc. Lond. Math. Soc.* **10**, 4–13.

Renardy, Y. 1985 Instability at the interface between two shearing fluids in a channel. *Phys. Fluids* **28**, 3411–3443.

Russo, M. J. & Steen, P. H. 1989 Shear stabilization of the capillary breakup of a cylindrical surface. *Phys. Fluids* A **1**, 1926–1937.

Saad, Y. 1980 Variations on Arnoldi's method for computing eigenelements of large unsymmetric matrices. *Linear Alg. Appl.* **34**, 269–295.

Santos, J. M. de, Melli, T. R. & Scriven, L. E. 1991 Mechanics of gas-liquid flow in packed-bed contactors. *Ann. Rev. Fluid Mech.* **23**, 233–260.

Smith, M. K. 1989 The axisymmetric long-wave instability of a concentric two-phase pipe flow. *Phys. Fluids* A **1**, 494–506.

Tsamopoulos, J. A., Poslinski, A. J. & Ryan, M. E. 1988 Equilibrium shapes and stability of captive annular menisci. *J. Fluid Mech.* **197**, 523–549.

Xu, J. J. & Davis, S. H. 1985 Instability of thermocapillary jets with thermocapillarity. *J. Fluid Mech.* **161**, 1–25.

Yiantsios, S. G. & Higgins, B. G. 1988 Linear stability of plane Poiseuille flow of two superposed fluids. *Phys. Fluids* **31**, 3225–3238.

Yih, C. S. 1967 Instability due to viscosity stratification. *J. Fluid Mech.* **27**, 337–352.